HAL open science

The Essential Role of Westerly Wind Bursts in ENSO Dynamics and Extreme Events Quantified in Model "Wind Stress Shaving" Experiments

Sungduk Yu, Alexey Fedorov

▶ **To cite this version:**

Sungduk Yu, Alexey Fedorov. The Essential Role of Westerly Wind Bursts in ENSO Dynamics and Extreme Events Quantified in Model "Wind Stress Shaving" Experiments. Journal of Climate, 2022, 35 (22), pp.3919-3938. 10.1175/jcli-d-21-0401.1 . hal-03952900

HAL Id: hal-03952900

https://hal.science/hal-03952900

Submitted on 21 Feb 2024

HAL is a multi-disciplinary open access archive for the deposit and dissemination of scientific research documents, whether they are published or not. The documents may come from teaching and research institutions in France or abroad, or from public or private research centers.

L'archive ouverte pluridisciplinaire **HAL**, est destinée au dépôt et à la diffusion de documents scientifiques de niveau recherche, publiés ou non, émanant des établissements d'enseignement et de recherche français ou étrangers, des laboratoires publics ou privés.

The Essential Role of Westerly Wind Bursts in ENSO Dynamics and Extreme Events Quantified in Model "Wind Stress Shaving" Experiments

SUNGDUK YU[a] AND ALEXEY V. FEDOROV[a,b]

[a] Department of Earth and Planetary Sciences, Yale University, New Haven, Connecticut
[b] LOCEAN/IPSL, Sorbonne University, Paris, France

(Manuscript received 25 May 2021, in final form 13 July 2022)

ABSTRACT: Westerly wind bursts (WWBs)—brief but strong westerly wind anomalies in the equatorial Pacific—are believed to play an important role in El Niño–Southern Oscillation (ENSO) dynamics, but quantifying their effects is challenging. Here, we investigate the cumulative effects of WWBs on ENSO characteristics, including the occurrence of extreme El Niño events, via modified coupled model experiments within Community Earth System Model (CESM1) in which we progressively reduce the impacts of wind stress anomalies associated with model-generated WWBs. In these "wind stress shaving" experiments we limit momentum transfer from the atmosphere to the ocean above a preset threshold, thus "shaving off" wind bursts. To reduce the tropical Pacific mean state drift, both westerly and easterly wind bursts are removed, although the changes are dominated by WWB reduction. As we impose progressively stronger thresholds, both ENSO amplitude and the frequency of extreme El Niño decrease, and ENSO becomes less asymmetric. The warming center of El Niño shifts westward, indicating less frequent and weaker eastern Pacific (EP) El Niño events. Removing most wind burst–related wind stress anomalies reduces ENSO mean amplitude by 22%. The essential role of WWBs in the development of extreme El Niño events is highlighted by the suppressed eastward migration of the western Pacific warm pool and hence a weaker Bjerknes feedback under wind shaving. Overall, our results reaffirm the importance of WWBs in shaping the characteristics of ENSO and its extreme events and imply that WWB changes with global warming could influence future ENSO.

KEYWORDS: El Niño; ENSO; Extreme events; Wind bursts; Climate change; Coupled models

1. Introduction

Episodic zonal wind anomalies, commonly known as westerly wind bursts (WWBs; also called westerly wind events) are frequently observed in the equatorial Pacific during El Niño events, in particular during extreme events such as those in 1982, 1997, and 2015 (Fig. 1). The occurrence of WWBs depends on a variety of phenomena whose time scales are shorter than El Niño–Southern Oscillation (ENSO), including the Madden–Julian oscillation (Yu and Rienecker 1998; Lau et al. 1989; Seiki and Takayabu 2007a,b; Chiodi et al. 2014; Puy et al. 2016; Feng and Lian 2018; Liang and Fedorov 2021), tropical cyclones (Keen 1982; Nitta 1989; Hartten 1996; Seiki and Takayabu 2007b,a; Lian et al. 2018b; Liang and Fedorov 2021), cold surges (Harrison 1984; Love 1985; Chu 1988; Yu and Rienecker 1998), and convectively coupled equatorial Rossby waves (Puy et al. 2016).

Having dominant time scales much shorter than ENSO time scales, WWBs provide stochastic forcing to ENSO (Harrison and Luther 1990; Harrison and Giese 1991). In idealized coupled ocean–atmosphere models with a damped ENSO mode such forcing helps sustain an irregular, quasi-periodic oscillation (Penland and Sardeshmukh 1995; Moore and Kleeman 1999; Thompson and Battisti 2001; Fedorov 2002; Fedorov et al. 2003). However, isolating the effects of intrinsic, model-generated WWB in comprehensive, fully coupled global climate models remains a difficult task (e.g., Guilyardi et al. 2012; An et al. 2021; Fedorov et al. 2021). The goal of this study is to quantify these effects using coupled model experiments specifically designed to reduce WWB impacts on the ocean.

As an important component of ENSO dynamics, WWBs affect equatorial sea surface temperature (SST) locally by generating anomalous eastward surface currents and remotely by exciting downwelling Kelvin waves propagating along the thermocline (McPhaden et al. 1988; Delcroix et al. 1993; Picaut and Delcroix 1995; McPhaden and Yu 1999; Lengaigne et al. 2002). Such dynamical effects, leading to the warming of the central and eastern equatorial Pacific respectively, contribute to the development of El Niño events, and some studies highlighted a potential role of WWBs as an early onset mechanism for extreme El Niño events (Fedorov 2002; Fedorov et al. 2015; Hu and Fedorov 2019; Latif et al. 1988; Lengaigne et al. 2004; Luther et al. 1983; McPhaden 1999; Perigaud and Cassou 2000; Puy et al. 2019).

As more frequent and stronger WWBs are observed over an anomalously warm ocean surface, state-dependent WWBs are suggested to play a role in the critical positive ocean–atmosphere feedback, the Bjerknes feedback (Bjerknes 1969), at intraseasonal time scales (McPhaden 1999; Vecchi and Harrison 2000; Yu et al. 2003; Lengaigne et al. 2004; Eisenman et al. 2005; Tziperman and Yu 2007; Seiki and Takayabu 2007a; Levine et al. 2017; Hu and Fedorov 2019). Relatedly, the fact that WWBs can influence important characteristics of ENSO

Supplemental information related to this paper is available at the Journals Online website: https://doi.org/10.1175/JCLI-D-21-0401.s1.

Corresponding author: Sungduk Yu, sungduk.yu@yale.edu

DOI: 10.1175/JCLI-D-21-0401.1

© 2022 American Meteorological Society. For information regarding reuse of this content and general copyright information, consult the AMS Copyright Policy (www.ametsoc.org/PUBSReuseLicenses).

Unauthenticated | Downloaded 02/21/24 12:34 PM UTC

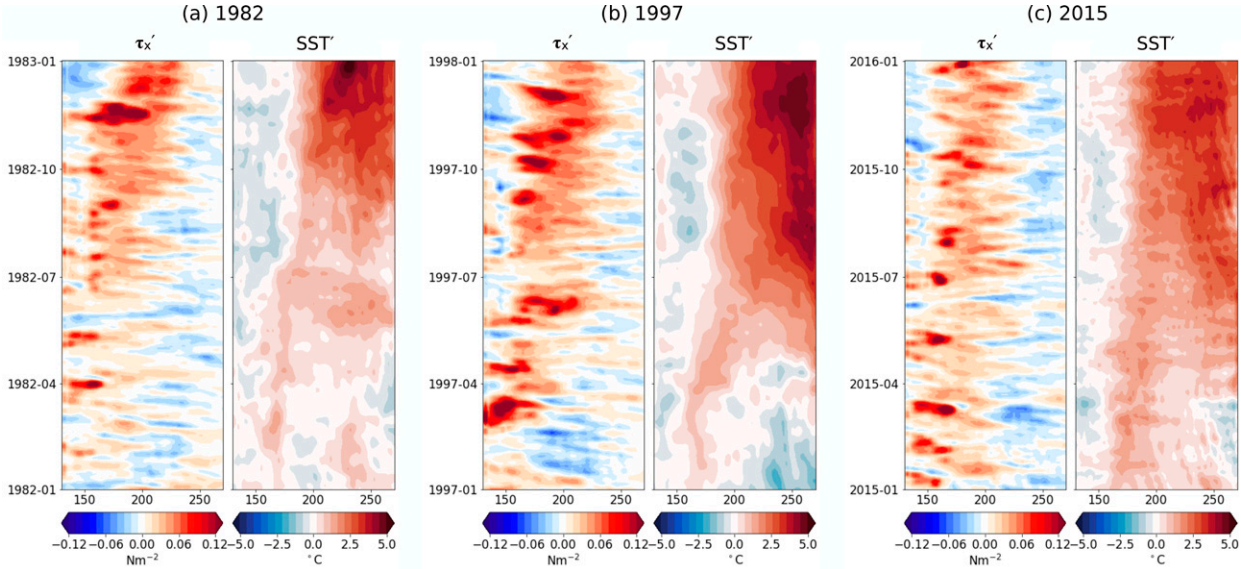

FIG. 1. Hovmöller diagrams of anomalous daily zonal surface wind stress (τ_x') and anomalous daily sea surface temperature (SST′) in the equatorial Pacific Ocean (2°S–2°N) for three extreme El Niño events in (a) 1982, (b) 1997, and (c) 2015. A 5-day running mean is applied. Data are from ERA-Interim (Dee et al. 2011).

(e.g., its magnitude, irregularity, asymmetry, and spatial diversity) has been shown in a hierarchy of models, including conceptual models (e.g., Jin et al. 2007; Levine and Jin 2010; Thual et al. 2016; Levine et al. 2016), intermediate models (e.g., Zavala-Garay et al. 2003; Eisenman et al. 2005; Perez et al. 2005), hybrid models (e.g., Gebbie et al. 2007; Zavala-Garay et al. 2008), and global climate models (GCMs; discussed next).

So far, there have been several approaches to investigate the role of WWBs in ENSO using ocean–atmosphere coupled GCMs. One approach is to perform initialized ensemble simulations with prescribed individual WWBs (e.g., Lengaigne et al. 2004; Hu et al. 2014; Fedorov et al. 2015; Hu and Fedorov 2019; Puy et al. 2019; Yu and Fedorov 2020). These studies suggest that strong WWBs in the early year (i.e., winter and spring) may strengthen the magnitude of ensemble mean El Niño whereas the occurrence of strong WWBs during the rest of the year (i.e., throughout the development phase) is necessary for an extreme El Niño event to develop. That is, WWBs increase the chances of an extreme El Niño for a given ocean recharge state (Wyrtki 1975; Meinen and McPhaden 2000; Yu and Fedorov 2020). In addition, WWBs affect the spatial pattern of El Niño events; for example, when WWBs occur more frequently, the warming center of El Niño tends to locate farther east (Fedorov et al. 2015). These types of studies using ensemble simulations allow us to examine the effects of WWBs amidst the internal variability of the climate system and show for example that El Niño development may still be uncertain even after strong early-year WWBs and a high ocean recharge, as demonstrated by the sharp contrast between years 2014 and 2015 (Larson and Kirtman 2015; Hu and Fedorov 2016; Levine and McPhaden 2016; Hu and Fedorov 2019; Puy et al. 2019; Yu and Fedorov 2020).

The second approach to examine the role of WWBs in GCMs is by adding stochastic and possibly state-dependent WWBs to the wind field generated by the model itself. Since many GCMs do not simulate WWBs realistically (Seiki et al. 2011; Feng and Lian 2018; Lian et al. 2018a), imposing WWBs may improve the simulated ENSO. The effects of stochastic and state-dependent WWBs have been broadly studied in idealized modeling frameworks, including highly simplified models (e.g., Levine and Jin 2010; Thual et al. 2016; Levine et al. 2016), intermediate complexity models (e.g., Fedorov et al. 2003; Eisenman et al. 2005; Hayashi and Watanabe 2017; Lian et al. 2014; Chen et al. 2015), and hybrid coupled models (e.g., Gebbie et al. 2007; Gebbie and Tziperman 2009). More recently, this approach has been employed in comprehensive GCMs, such as CCSM3 and CCSM4 (e.g., Lopez and Kirtman 2014, 2013; Lopez et al. 2013) and CESM1.2 (e.g., Tan et al. 2020a,b).

Although previous studies imposing individual or stochastic WWBs confirm several important qualitative effects of WWBs in ENSO in comprehensive GCMs, quantifying the net impacts of WWBs on ENSO from those studies is difficult. The initialized ensemble approach helps examine the role of WWBs in individual El Niño events but not in ENSO long-term statistics. On the other hand, GCM studies with added state-dependent WWBs (wherein WWBs occurrence is tired to SST anomalies) allow assessing qualitative effects of added WWBs on ENSO statistics, but with several limitations. First, the imposed WWBs are not consistent with atmospheric circulation simulated by the model (in contrast to model-generated WWBs in our study). Second, adding state-dependent WWBs modifies the mean state of the equatorial Pacific and those mean state changes can affect ENSO, making the attribution of ENSO changes challenging. For example, in Community Earth System

Unauthenticated | Downloaded 02/21/24 12:34 PM UTC

Model 1.2 (CESM1.2; the same GCM as used in this study), imposing state-dependent WWBs causes nontrivial changes of the mean state including changes in zonal wind stress (e.g., reduced surface easterlies in the western/central Pacific up to 0.02 N m^{-2}) and thermocline depth (e.g., a shoaling of the western/central Pacific by more than 10 m) (Tan et al. 2020a). Finally, by construction imposing WWBs does not allow quantifying the effect of intrinsic WWBs in a freely run fully coupled GCM (Yu and Fedorov 2020).

Accordingly, in the present study, we develop a new method to quantify the effect of WWBs on both the long-term statistics of ENSO and extreme El Niño events and the development of individual events—by limiting the effect of intrinsic, model-generated WWBs yet keeping potential changes to the tropical Pacific mean state minimal. Our approach extends the approach of Puy et al. (2019), who experimented with the removal of strong WWBs in year-long initialized ensemble simulations. Specifically, we conduct a series of multicentury simulations using a fully coupled GCM (CESM1.2) in which we modify the effect of WWB wind stress on the ocean. We refer to our approach as "wind burst shaving" or "wind stress shaving" or simply the "wind shaving" method. In the wind shaving simulations, momentum transfer from the atmosphere to the ocean during wind bursts are selectively limited over the tropical Pacific, reducing wind stress anomalies acting on the ocean. As we reduce wind stress anomalies only during relatively short but intense wind bursts, any wind spikes are effectively "shaved off." Subsequently, the effects of WWBs on ENSO are examined in a suite of simulations with progressively stronger wind shaving. We note that, to reduce changes to the mean state, the wind shaving procedure is applied symmetrically (i.e., to both westerly and easterly wind bursts). However, it is WWBs that are predominantly shaved as they are typically stronger in magnitude (see section 5 for further discussion).

Even though our goals here are broadly aligned with the previous studies that used fully coupled GCMs, this study is novel as it aims to quantify the effect of intrinsic, model-generated WWBs on ENSO in a freely run fully coupled GCM. Furthermore, when mean surface winds are modified in coupled GCMs, the tropical ocean mean state can easily drift due to atmosphere–ocean interactions (e.g., with addition or removal of WWBs). In contrast, the wind shaving procedure affects the mean state minimally (see section 5 for further discussion). Thus, our approach allows us to attribute ENSO changes to WWBs and accurately quantify the effect of intrinsic, model-generated WWBs on ENSO. Besides, some of the following elements of our approach were present in previous studies, but this study is unique in that it combines all of those different elements. First, our simulations are sufficiently long (400 years) to robustly examine the effects of WWBs on the long-term statistics of ENSO and extreme El Niño events. Second, our study uses internally generated WWBs as opposed to superimposed WWBs. That is, unlike superimposed WWBs, simulated WWBs are part of the model's large-scale atmospheric variability. Moreover, while the representation of WWBs in the model is not bias-free, CESM1.2 does reproduce well the observed relationship between the likelihood of WWBs and the underlying SST [see discussions in section 3 herein and in Yu and Fedorov (2020)].

The rest of the article is organized as follows. Section 2 describes the details of the model and wind shaving simulations. Section 3 compares WWBs simulated by CESM1.2 and those in atmospheric reanalyses. Section 4 shows key results on how limiting WWBs by the wind shaving affects the characteristics (e.g., amplitude, asymmetry, and spatial diversity) of ENSO and the frequency of extreme El Niño. Section 5 includes a discussion of the effects of the wind shaving on the wind variability and background climate state of the equatorial Pacific. Section 6 summarizes the main findings.

2. Methods

The coupled climate model used in this study is described in section 2a. The details of the shaving method, including the model modification and the wind shaving threshold settings, are given in section 2b. The description of the control and perturbed simulations is given in section 2c.

a. *The global climate model*

The Community Earth System Model (CESM) version 1.2 developed by National Center of Atmospheric Research (Hurrell et al. 2013) is used for our study. The model resolution is 1.9° × 2.5° for the atmospheric and land components and nominally 1° × 1° (with a finer latitudinal increment near the equator) for the ocean and sea ice components. We employ a standard "B_1850_CAM5" configuration, which uses preindustrial radiative forcing. CESM1.2 captures the observed properties of ENSO relatively well, including ENSO amplitude, seasonality (Bellenger et al. 2014), and asymmetries (DiNezio et al. 2017), showing improvement of the simulated ENSO over its predecessors (e.g., CCSM3 and CCSM4; Zhang et al. 2017; Capotondi et al. 2020).

b. *The wind stress shaving approach*

The aim of the wind shaving procedure is to reduce wind stress anomalies that the ocean feels when and where WWBs occur. We implement this procedure during the coupling processes at the end of each day of model integration, so that the atmospheric and ocean models share the same surface state throughout model integration. In the absence of wind shaving modifications surface ocean–atmosphere momentum fluxes are coupled as follows (Fig. 2a): 1) the coupler receives surface winds from the atmospheric model and surface currents from the ocean model, 2) the atmospheric wind field is remapped onto the grid of the ocean model, 3) the coupler calculates surface wind stress using a bulk formula, and 4) the calculated wind stress is sent back to the ocean and the atmospheric models (in the latter case, it is remapped onto the atmospheric grid).

To limit anomalous zonal momentum transfer from the atmosphere to the ocean, we intervene in step 4 (bold arrow in Fig. 2a). Once the coupler calculates zonal wind stress τ_x, the anomalous zonal wind stress τ_x' relative to the climatological

Unauthenticated | Downloaded 02/21/24 12:34 PM UTC

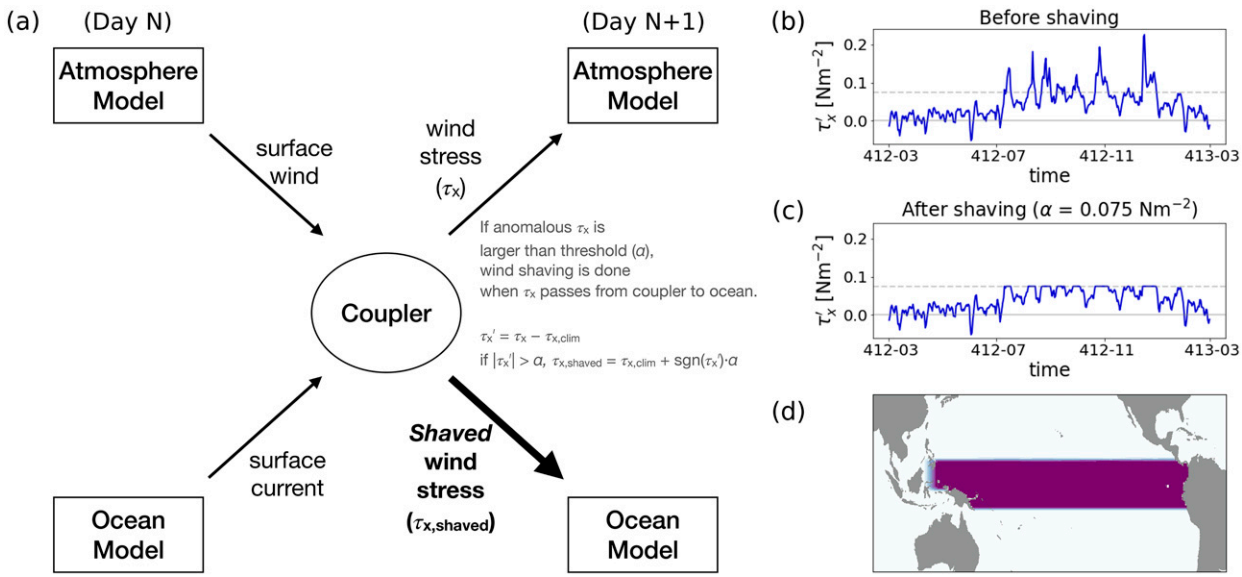

FIG. 2. (a) A schematic of the wind shaving method. Wind stress is modified within the model coupler before being sent to the ocean model (see section 2 for details). (b),(c) An example of wind shaving, with threshold $\alpha = 0.075$ N m^{-2}, applied during an extreme El Niño event randomly chosen from the control simulation. These two panels show zonal wind stress anomalies (blue lines) relative to the model daily climatology, averaged over the central equatorial Pacific (2°S–2°N, 190°–205°E), before and after the shaving. Gray dashed lines indicate threshold α. (d) The region where wind shaving is applied. The wind shaving magnitude is tapered off at the boundaries except in the very east.

annual cycle of daily zonal wind stress $\overline{\tau}_x$ is computed (i.e., $\tau_x' = \tau_x - \overline{\tau}_x$). Then, the magnitude of the anomalous zonal wind stress $|\tau_x'|$ is replaced by a preset threshold α if $|\tau_x'|$ is larger than α. This procedure is summarized as follows:

$$\tau_{x,\text{shaved}} = \begin{cases} \overline{\tau}_x + \alpha, \text{ if } \tau_x' > \alpha; \\ \tau_x, \text{ if } \alpha \geq \tau_x' > -\alpha; \\ \overline{\tau}_x - \alpha, \text{ if } \tau_x' \leq -\alpha. \end{cases} \quad (1)$$

Note that $\tau_{x,\text{shaved}}$ is sent back only to the ocean model as the wind shaving procedure is applied only to wind stress that the ocean feels. Following this expression, both westerly and easterly wind bursts (WWBs and EWBs) are shaved to reduce potential changes to the ocean mean state. Implications of this symmetric wind shaving are discussed in section 2d.

The wind shaving procedure modifies only the zonal component of surface wind stress. Even though twin vortices are often observed during WWB episodes, their meridional wind stress anomalies are very small in the vicinity of the equator (5°S–5°N) in comparison with zonal wind stress anomalies [see Fig. 4 in Puy et al. (2016) or Fig. 6 in Hu and Fedorov (2019)]. Therefore, keeping meridional wind stress anomalies associated with wind bursts unchanged should not impact the results of our study.

Figures 2b and 2c demonstrate how the wind shaving works. Figure 2b shows equatorial τ_x' averaged over 190°–205°E during a randomly picked extreme El Niño event from the control simulation, while Fig. 2c shows τ_x' after wind shaving has been applied using threshold $\alpha = 0.075$ N m^{-2}. The shaving is applied at each grid cell of the model across the tropical Pacific (10°S–10°N) as shown on the map in Fig. 2d. The wind shaving is tapered off at the margins of the tropical Pacific domain except at the eastern boundary. For tapering at the northern and southern boundaries we use tanh functions; for example, the fraction of wind shaving applied is computed as $0.5\{\tanh[1.25(\phi + 10°)] - \tanh[1.25(\phi - 10°)]\}$, where ϕ is latitude in degrees. At the western boundary we use a linear taper, namely $(\lambda - 118°)/10°$ for $118° \leq \lambda < 128°$, where λ is longitude in degrees east.

To quantify the effects of WWBs, selecting an appropriate wind shaving threshold is crucial. A too large value of the threshold α would remove WWBs only partially; this can be used to examine the effect of WWBs by gradually decreasing α. However, a too small value of α would cause the shaving procedure to affect slower wind stress variations on interseasonal and longer time scales coupled to variations in the zonal SST gradient during El Niño development, thus going beyond our intent to selectively reduce WWB wind stress only.

To decide on the choice of α, let us consider the Control run first. Following Puy et al. (2016), we define WWB as westerly wind stress anomalies longer than 5 but shorter than 90 days (within the intraseasonal range). We also require their zonal extent be greater than 12.5°. Finally, we require their magnitude to be greater than a preset threshold α. Figure 3 shows examples of the time–longitude structure of WWBs during a randomly chosen extreme El Niño event in the control simulation (the same event as in Fig. 2b) for four different thresholds ($\alpha = 0.1$, 0.075, 0.05, and 0.04 N m^{-2}). These examples suggest that making the threshold smaller

Unauthenticated | Downloaded 02/21/24 12:34 PM UTC

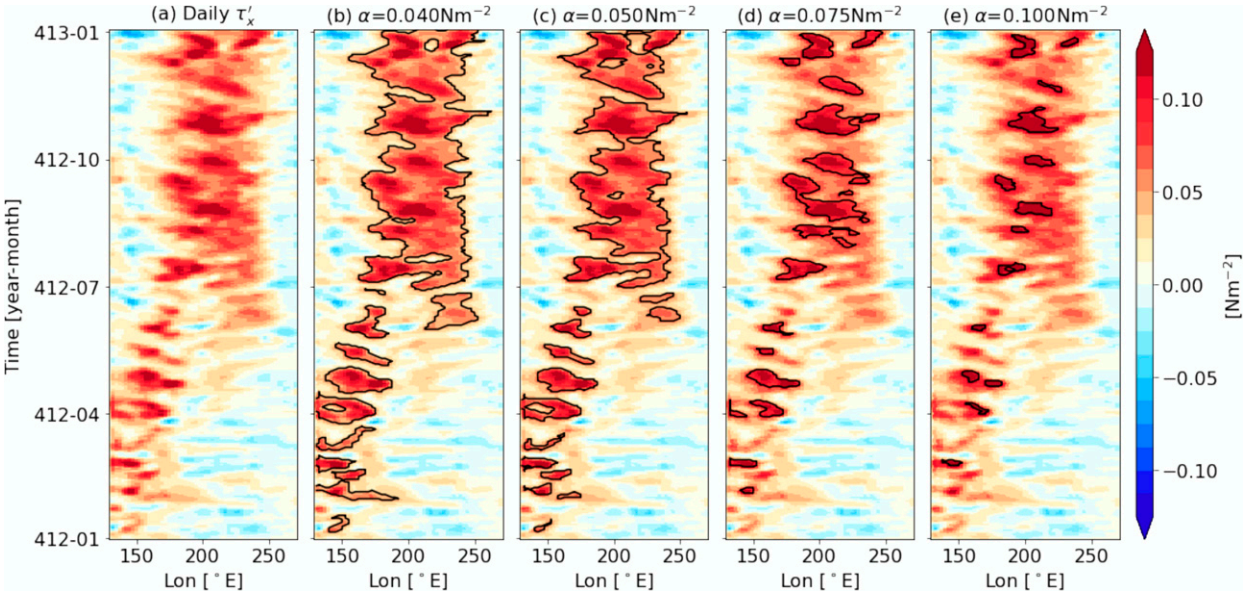

FIG. 3. (a) Hovmöller diagrams of daily equatorial (2°S–2°N) zonal wind stress anomalies generated by the atmospheric component of the model during the same El Niño event as shown in Fig. 2b. (b)–(e) As in (a), but with black contours identifying WWWs in accordance with different thresholds α: α = 0.04, 0.05, 0.075, and 0.1 N m^{-2}, respectively. Choosing thresholds below 0.05 N m^{-2} may combine shorter wind bursts into events longer than 3–4 months, which implies that the wind shaving procedure using small threshold values could start removing wind variations longer than WWBs. A 5-day running mean is applied to the data.

than 0.05 N m^{-2} may result in some of the bursts being longer than 90 days.

To investigate this issue further we apply these different thresholds to the 400-yr control simulation and combine the durations of WWBs into a histogram (Fig. 4). The total number of the detected WWBs increases for smaller α as one would expect, while the probability of too long WWB remains low for all these threshold values (Figs. 4a–d). To better visualize the distribution of WWBs for longer durations, the distribution tails are displayed in Figs. 4e–h. As the threshold decreases, the maximum duration of the identified WWBs increases and the tail of probability distribution extends further. For example, WWB detection using the 0.1 and 0.075 N m^{-2} thresholds yields wind bursts all shorter than 60 days, but 0.04 N m^{-2} threshold includes a few WWBs with longer durations. The 0.05 N m^{-2} threshold produces several WWBs lasting beyond 60 days, but their occurrence is very rare: for this threshold, out of 2028 WWBs identified in the 400-yr simulation only 11 wind bursts are longer than 60 days and only 7 longer than 90 days. Therefore, we use the 0.1, 0.075, and 0.05 N m^{-2} thresholds in our wind shaving experiments to successively reduce wind stress anomalies associated with WWBs, and we consider the 0.05 N m^{-2} threshold to be close to a critical value that allows removing most of WWB cumulative wind stress effects without affecting interseasonal wind stress variations.

c. Simulations

Although CESM provides spun-up initial conditions, we first run the model for additional 350 years to finish the spinup. The first day of year 351 is then used for initializing both the control and the wind shaving experiments, which are integrated for 400 years. The control simulation is used to compute the climatological annual cycle of daily zonal surface wind stress (i.e., $\overline{\tau}_x$ in section 2b) necessary for the wind shaving procedure.

The wind shaving simulations are integrated for three different wind shaving thresholds as described in the previous subsection: α = 0.1, 0.075, and 0.05 N m^{-2}. We refer to these simulations, reflecting different strengths of wind shaving, as weak shaving (α = 0.1 N m^{-2}), moderate shaving (0.075 N m^{-2}), and strong shaving (0.05 N m^{-2}).

For our analysis, we retain the entire 400 years of each experiment since there is no significant mean state drift in the tropical Pacific even in the beginning of the perturbed simulations (Fig. S1 in the online supplemental material). The absence of initial mean climate drift is likely due to the episodic—not constant—nature of wind shaving that affects the system only during ENSO events.

d. Validation of the wind stress shaving procedure

In this subsection, we demonstrate that our wind stress shaving procedure affects predominantly WWBs, not EWBs, despite the fact that the wind stress shaving limits both westerly and easterly wind stress anomalies symmetrically; that is, the same threshold is applied to both positive and negative wind stress anomalies.

Figure S2 shows the histograms of EWB durations detected from the 400-yr control simulation (cf. Fig. 4 for WWBs). We find that applying weaker thresholds leads to predominant detection of WWBs. For example, the fraction of detected EWBs relative to WWBs is approximately 0.3% and 13% for

Unauthenticated | Downloaded 02/21/24 12:34 PM UTC

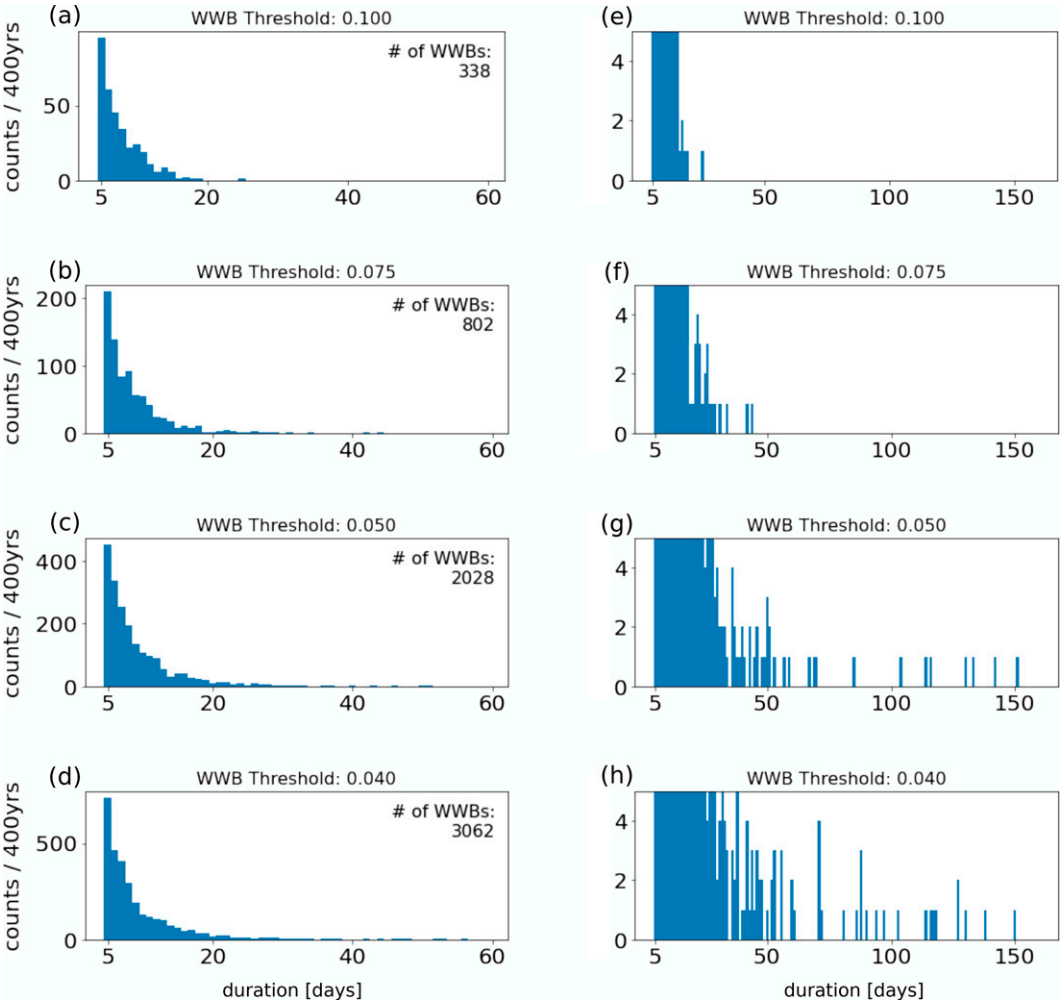

FIG. 4. A histogram of durations of individual WWBs corresponding to four different thresholds α used to isolate wind bursts: (a) 0.1, (b) 0.075, (c) 0.05, and (d) 0.04 N m^{-2}. (e)–(h) As in (a)–(d), but visualizing the distribution tails. The wind burst duration is computed using zonal wind stress anomalies, relative to the model daily climatology, averaged over the central equatorial Pacific (2°S–2°N, 190°–205°E). Each simulation lasts 400 years. The total number of wind bursts detected during 400 years is shown at the top right corner of each panel. Note that a vast majority of wind bursts defined using these thresholds are shorter than 60 days; however, the number of longer bursts starts increasing when the threshold is smaller than 0.05 N m^{-2}. A similar figure for EWBs is included in the online supplemental material (Fig. S2).

the 0.10 and 0.075 N m^{-2} thresholds, respectively. Accordingly, in these simulations ENSO is predominantly affected by the shaving of WWBs. The fraction of EWBs increases to 74% when using the 0.05 N m^{-2} threshold. This rise likely results from the quadratic bulk formula for wind stress and the dominance of mean easterly winds in the equatorial Pacific (Hayashi and Watanabe 2016). Nevertheless, even for this stricter threshold the accumulated wind stress forcing due to EWBs reaches only 52% or 42% (after normalization) of that due to WWBs (Fig. S3). Thus, given this weaker accumulated forcing and generally weaker dynamical effects of EWBs, we expect the impacts of WWB removal to dominate the results.

We note that the effects of the wind stress shaving procedure are concentrated along the equator, although the wind stress shaving is applied for a broader equatorial region (10°S–10°N). Figure 5 shows the daily-averaged magnitude of shaved τ_x during WWB and EWB episodes, after normalizing by the annual climatology of zonal surface wind stress, that is,

$$\frac{\int(|\tau'_{x,\mathrm{WWB(EWB)}}|)|\tau_{x,\mathrm{clim}}|^{-1}dt}{\int dt}, \tag{2}$$

where $\tau'_{x,\mathrm{WWB(EWB)}}$ is τ'_x during WWB or EWB episodes defined by threshold α, and $\tau_{x,\mathrm{clim}}$ is the annual daily climatology of τ_x. This figure confirms that the effect of wind shaving is mostly confined near the equator, which assures that we mainly limit WWBs in the vicinity of the equator, and not off-equatorial wind stress anomalies around the chosen boundaries

Unauthenticated | Downloaded 02/21/24 12:34 PM UTC

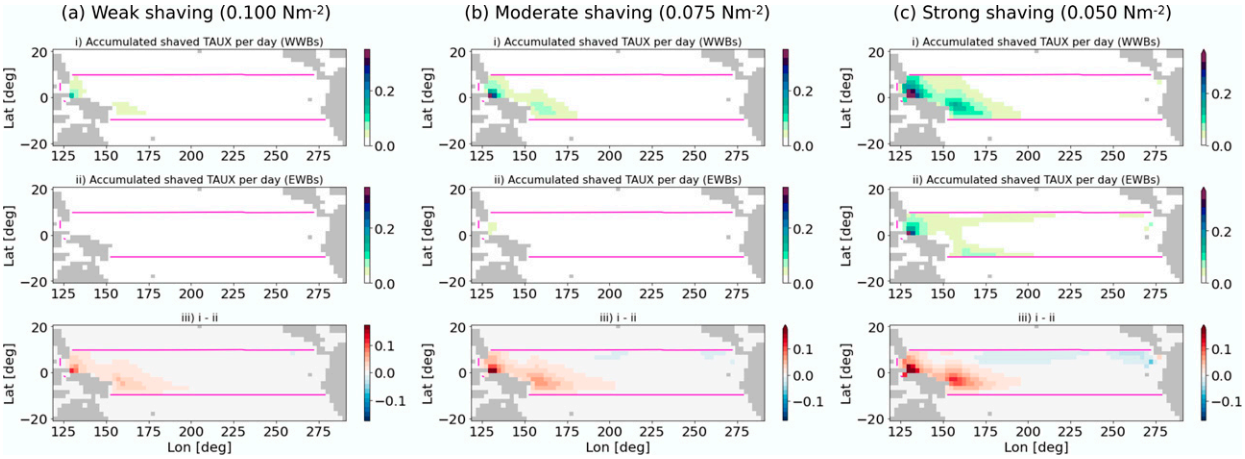

FIG. 5. Normalized daily-mean accumulated τ_x' of (i) shaved WWBs, (ii) shaved EWBs, and (iii) the difference, that is, (i) minus (ii), for the (a) weak, (b) moderate, and (c) strong shaving experiments. The values shown are normalized by the annual daily climatology of zonal surface wind stress, see Eq. (2). A version of this plot without normalization is provided in Fig. S4. In effect, since the accumulated τ_x' of EWBs is small, bottom panels show the average horizontal distribution of shaved WWBs.

of the tropical domain (Fig. 2d), which could produce spurious wind stress forcing.

3. WWBs in CESM1.2 versus atmospheric reanalyses

Since the wind shaving simulations modify WWBs internally generated by the model, we briefly examine how well WWBs are simulated in the control simulation of CESM1.2 as compared to the observations. Two atmospheric reanalysis products are used to characterize the observed WWBs: ERA-Interim (Dee et al. 2011) and MERRA-2 (Gelaro et al. 2017), which span 40 (1979–2018) and 39 (1980–2018) years, respectively. The ERA-Interim and MERRA-2 datasets are interpolated to the atmospheric model grid of CESM1.2 before extracting WWBs.

WWBs are identified as described in section 2b. The model and the two reanalyses have somewhat different magnitudes of daily surface wind stress variability: the standard deviation of daily τ_x' in the central equatorial Pacific (an average of grid-wise standard deviation over 2°S–2°N and 160°–210°E) is 0.028, 0.030, and 0.034 N m^{-2} for the CESM1.2 control simulation, ERA-Interim, and MERRA-2, respectively. Consequently, the magnitude threshold for wind bursts is set individually in each dataset at 1.77 times the standard deviation (based on the threshold in the strong-shaving experiment, 0.050 N m^{-2}). For dataset comparison, we use a normalized strength of WWBs (hereafter simply WWB strength). It is calculated by (i) integrating τ_x' of identified WWBs ($\tau_{x,\mathrm{WWB}}'$) in space over equatorial Pacific basin and in time and then (ii) normalizing by grid cell area (ΔA), time resolution (Δt; one day in this case), and standard deviation (σ_τ); that is, WWB strength $= (\Delta A\ \Delta t\ \sigma_\tau)^{-1} \int\int \tau_{x,\mathrm{WWB}}' dA dt$.

The annual cycle of monthly-integrated WWB strength over the equatorial Pacific is shown in Fig. 6a. While the ERA-Interim (magenta line) and MERRA-2 (cyan line) results are computed as climatology for their entire periods of the data (40 and 39 years, respectively), results from the control simulation are shown for the median (gray line) and 95% confidence interval (gray shading; the range is between the 2.5th and the 97.5th percentiles) as estimated from a 100 000 block bootstrap resampling of 40-yr segments with 30-yr overlaps.

In general, CESM1.2 simulates a gradual reduction of WWBs in winter and a strengthening of WWBs toward the end of the year, similar to ERA-Interim and MERRA-2. However, the two observational data products show a much stronger annual cycle in the strength of WWBs, including a significant midyear reduction in WWBs that the model does not replicate. This issue can be due to model mean state biases and/or due to a sampling bias related to the short length of the observational data—that is, there are only four observed El Niño events with the November–January (NDJ) mean Niño-3 index above one standard deviation of about 1.2°C (the events of 1982/83, 1991/92, 1997/98, and 2015/16), while in the model strong events are more frequent and responsible for a large fraction of generated WWBs (Yu and Fedorov 2020).

On the other hand, CESM1.2 can reproduce the modulation of WWBs by SST reasonably well, as compared to ERA-Interim and MERRA-2. Figures 6b–d show the longitudinal profiles of average monthly WWB strength based on the location of the eastern boundary of the tropical Pacific warm pool for the control simulation and the reanalyses; the warm pool edge is defined by the location of the 28°C isotherm. Only El Niño years are included in Figs. 6b–d (when the Niño-3 index averaged for NDJ is greater than one standard deviation). Consistent with ERA-Interim and MERRA-2, WWBs in CESM1.2 become stronger and migrate eastward as the warm pool shifts eastward as part of El Niño development. Nevertheless, there are some minor differences between CESM1.2 and the reanalysis data. For example, CESM1.2 shows zonally broader WWB activity at the peak of El Niño events (i.e., when the warm pool reaches the eastern Pacific; brown lines

Unauthenticated | Downloaded 02/21/24 12:34 PM UTC

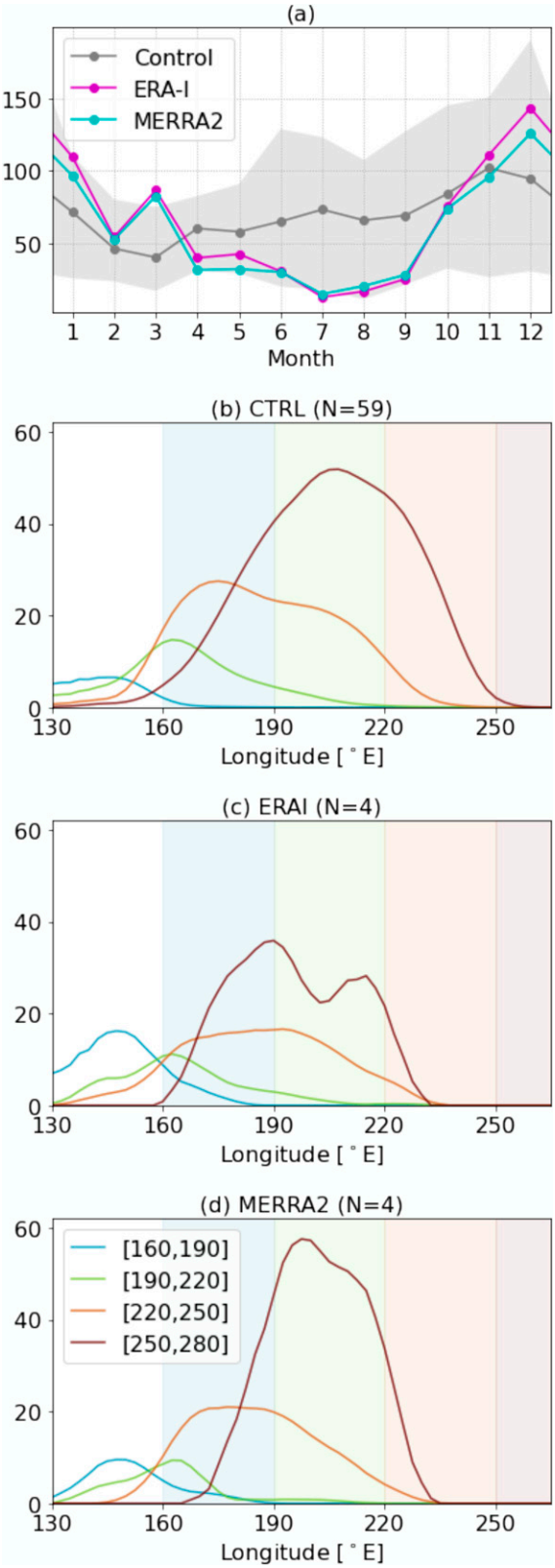

FIG. 6. (a) Climatological annual cycle of monthly WWB strength summed over the equatorial Pacific basin for the control (gray), and atmospheric reanalyses ERA-Interim (magenta) and MERRA-2 (cyan). While ERA-Interim and MERRA-2 are shown for the climatological average of the entire dataset period of 40 and 39 years, respectively, the control simulation is shown for its median (gray line) with the 95% confidence interval (gray shading). WWBs are defined as events whose magnitude, duration, and zonal extent of anomalous surface zonal wind stress in the equatorial Pacific (2°S–2°N) are greater than 1.77 times the standard deviation of central equatorial wind stresses, 5 days, and 12.5°, respectively. The confidence interval is estimated by 100 000 block bootstrap resampling with 40-yr segments with 30-yr overlaps. The zonal structure of WWBs binned by the longitudinal location of the eastern edge of the western Pacific warm pool (28°C) during moderate El Niño years (NDJ Niño-3 index greater than one standard deviation) for (b) the control simulation, (c) ERA-Interim, and (d) MERRA-2. The number of qualified El Niño events is 58, 4, and 4 for the control simulation, ERA-Interim, and MERRA-2, respectively. The four bins are bounded by longitudes 160°, 190°, 220°, 250°, and 280°E and are marked by background color shadings. WWBs typically occur to the west of the warm pool eastern edge.

in Figs. 6b–d). This is likely due to the model's ENSO SST variability being stronger than the observed (DiNezio et al. 2017). Another difference is a weaker WWB activity in the western Pacific when the warm pool stays in the western Pacific (light blue lines in Figs. 6b–d). These differences however might stem from (i) the observational record being too short, since only four qualified El Niño events are used for the ERA-Interim and MERRA-2 composites compared to 59 events for CESM1.2 and/or (ii) other common coupled GCM biases, such as the so-called cold tongue SST and double intertropical convergence zone biases (Mechoso et al. 1995; Lin 2007; Li and Xie 2014; Burls et al. 2017; Thomas and Fedorov 2017; Tian and Dong 2020).

4. Results of perturbation experiments

Here, we discuss the systematic weakening of ENSO (section 4a) and the reduced occurrence of extreme El Niño events (section 4b) under the wind shaving procedure. Individual El Niño events across different perturbation experiments are compared in section 4c and the WWB–warm pool feedback is discussed in section 4d. In all our analyses, anomalies (denoted by primes) are defined with respect to the climatology of each simulation. Zonal wind stress (τ_x) comes from the atmospheric model unless mentioned otherwise; when necessary, we use the subscript "atm" (e.g., $\tau_{x,\mathrm{atm}}$) to avoid confusion. Zonal wind stress from the ocean model is always denoted by the subscript "ocn" (e.g., $\tau_{x,\mathrm{ocn}}$). We remind the reader that we only modify zonal wind stress that the ocean feels ($\tau_{x,\mathrm{ocn}}$), while zonal wind stress computed within the atmospheric model ($\tau_{x,\mathrm{atm}}$) remains unaltered.

a. Reduction of ENSO amplitude

To demonstrate the response of ENSO to the wind shaving we first consider the standard deviation of daily τ_x' and SST′ in the equatorial Pacific, which clearly shows that ENSO weakens in the wind shaving experiments (Fig. 7). Variability

Unauthenticated | Downloaded 02/21/24 12:34 PM UTC

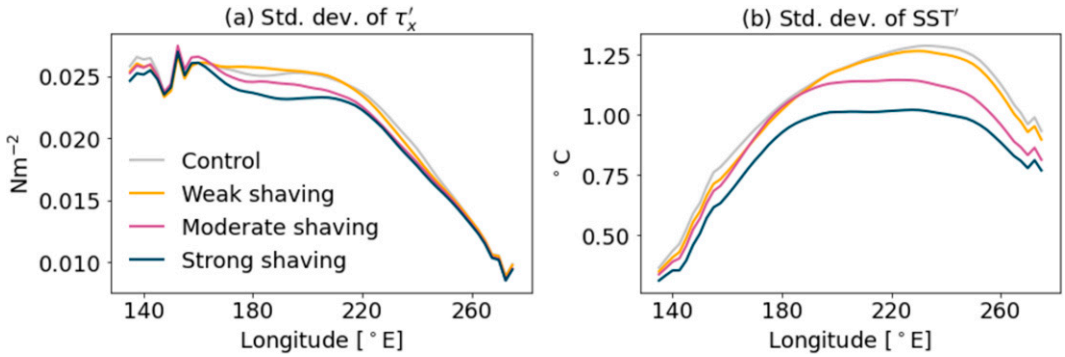

FIG. 7. Standard deviation of daily anomalies of (a) zonal surface wind stress and (b) SST along the equator (averaged 5°S–5°N). Zonal surface wind stress anomalies are from the atmospheric model, i.e., not shaved. Note the monotonic reduction in STD as more of the WWB wind stress effect on the ocean is eliminated. The largest reduction of SST variance happens in the eastern Pacific.

of both τ_x' and SST′ becomes smaller monotonically as the wind shaving intensifies. ENSO SST anomalies in the eastern Pacific appear to be more sensitive to the imposed changes than those in the central Pacific, indicating that the spatial patterns of El Niño are affected by WWBs.

Since the largest reduction of variability for τ_x' is centered around the Niño-4 region (160°–210°E, 5°S–5°N) and for SST′ around the Niño-3 region (210°–270°E, 5°S–5°N), next we consider changes in the standard deviations of these two variables averaged for the respective region (Fig. 8). The standard deviation of Niño-3 SST′ is reduced to 97.9%, 87.4%, and 78.4% in the weak, moderate, and strong shaving simulations, respectively.

Changes of τ_x' variability over the Niño-4 region are smaller (100.7%, 97.0%, and 94.0%); the slight 0.7% increase of τ_x' variability relative to the control in the strong shaving simulation is statistically insignificant (p value = 0.2) based on an F test with an effective number of degrees of freedom of 14 600. Since τ_x in the atmosphere model is not shaved, changes in τ_x' magnitude are caused by the general weakening of ENSO in the wind shaving experiments. The smaller sensitivity of the atmospheric τ_x' variability, as compared to SST′, confirms that the wind shaving approach does not dampen intraseasonal atmospheric surface wind variability directly. A further discussion of the response of atmospheric surface wind variability is provided in section 5.

As indicated by the greater reduction in SST variability in the eastern Pacific than in the central Pacific (Fig. 7b), the warming center of El Niño shifts westward under the action of wind shaving. Scatterplots connecting Niño-4 and Niño-3 SST indices for NDJ after normalized by the standard deviation of the control simulation confirm this shift (Figs. 9a–c). The relative magnitudes of the Niño-4 and Niño-3 indices provide a simple classification of the spatial pattern of El Niño events: the central Pacific (CP) type if Niño-4 > Niño-3 and the eastern Pacific (EP) type if Niño-3 > Niño-4 (Kug et al. 2009; Hu et al. 2014; Fedorov et al. 2015; Capotondi et al. 2015). We find that the westward shift of the El Niño warming center (Fig. 7b) corresponds to reduction in both intensity and frequency of EP El Niño events (Figs. 9d,e), while changes in the frequency of CP events do not show any robust trend.

b. *Reduced frequency and intensity of extreme El Niño events*

Limiting the momentum transfer from WWBs to the ocean by the wind shaving procedure reduces the frequency and typical intensity of extreme El Niño events as the histograms of

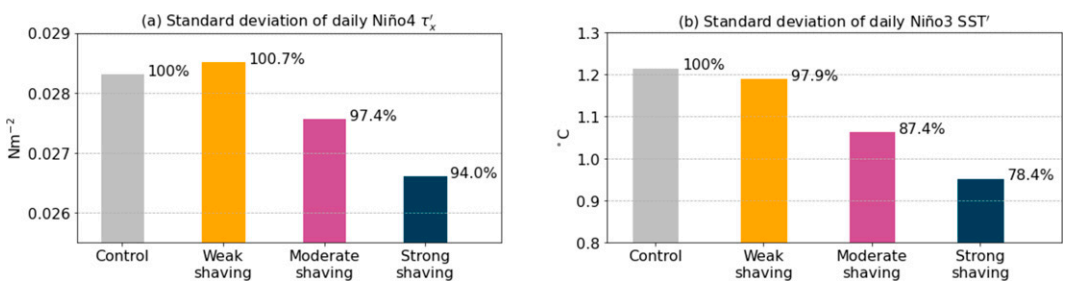

FIG. 8. Standard deviation of daily (a) Niño-4 zonal surface wind stress anomalies and (b) Niño-3 SST anomalies. For (a) only, the standard deviation is calculated at each grid cell and then averaged over the Niño-4 region. Percentage values relative to the control simulations are shown at the top of each bar. The slight increase in the wind stress STD over the Niño-4 region in the weak shaving experiment is compensated by the STD reduction over the Niño-3 region (Fig. 7).

Unauthenticated | Downloaded 02/21/24 12:34 PM UTC

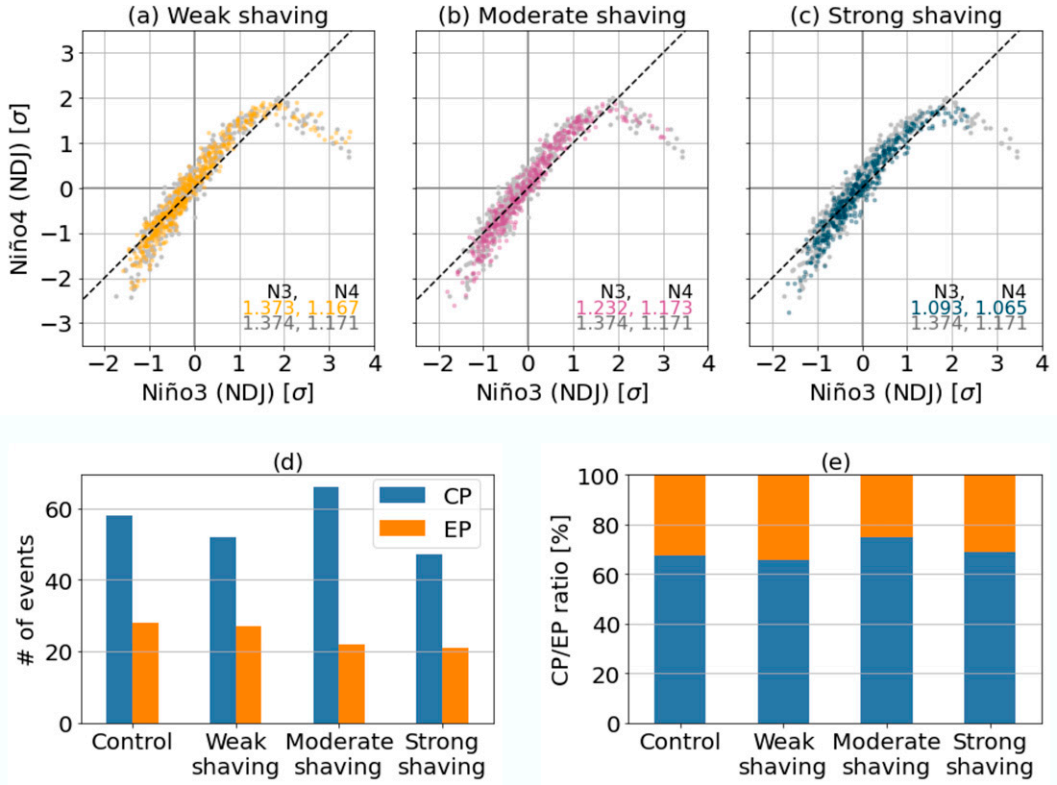

FIG. 9. Scatterplots connecting Niño-4 (on the y axis) and Niño-3 (on the x axis) SST indices for the (a) weak, (b) moderate, and (c) strong shaving simulations. The indices are averaged for NDJ and normalized by the standard deviations of the control simulation (σ). The control simulation is shown in gray. The dashed line shows a one-to-one line. The standard deviations of NDJ-mean Niño-3 and Niño-4 indices are shown at the bottom right corner of each panel. (d),(e) The total number and the relative fraction of CP and EP El Niño events, respectively, following the classification of Kug et al. (2009).

the NDJ Niño-3 SST index show (Fig. 10). The medians and 90% confidence intervals (ranges between the 5th and the 95th percentiles) are estimated by a 100 000-block bootstrap resampling of 100-yr segments with an 80-yr overlap. For further comparison, we define extreme El Niño events in the model as events with the NDJ Niño-3 index greater than 3.5°C, which corresponds to roughly 2.5 times the standard deviations of the NDJ Niño-3 index in the control simulation. The frequency of extreme El Niño events diminishes monotonically with the strength of wind stress shaving. For example, while the weak-shaving simulation does not exhibit distinguishable changes in the frequency of extreme El Niño events, the moderate- and strong-shaving experiments are unable to simulate extreme El Niño events with the NDJ Niño-3 index greater than 4.5° and 3.5°C, respectively (such events are present in the 400-yr control simulation).

Along with the frequency of extreme El Niño events, the frequency of strong La Niña events also responds to the wind stress shaving procedure. While no noticeable changes are seen in the weak and moderate shaving experiments, the strong shaving experiment demonstrates a clear reduction in La Niña events colder than −1.5°C. We speculate about two possible causes of the reduction of strong La Niña events. First, although our wind shaving procedure predominantly limits WWBs, and not EWBs, the shaving of the EWBs might still play a role; however, the effect of EWBs on the development of La Niña has not been studied extensively, and the existing studies disagree on their impacts (Chiodi and Harrison 2015; Puy et al. 2016). Second, the reduction of strong El Niño events could be important, given that strong La Niña events usually follow strong El Niño events and the subsequent ocean heat discharge. A simple analysis of the equatorial ocean heat content gives weight to the latter hypothesis. As expected, we find that after strong El Niño events, the equatorial Pacific experiences a large ocean heat discharge (Fig. S5). With the reduction in extreme El Niño event occurrence, episodes of such large heat discharge become less frequent, especially in the moderate and strong shaving simulations. However, this link is only tentative as in this model strong La Niña events can still occur even after a weak heat discharge (Fig. S6), and therefore a further analysis is required to confirm this hypothesis.

The reduced frequency of extreme El Niño events makes the equatorial eastern Pacific SST distribution less asymmetric as seen from the histograms of 3-month moving-averaged SST for the Niño-3 region (Fig. 11). The frequency of extreme El Niño

Unauthenticated | Downloaded 02/21/24 12:34 PM UTC

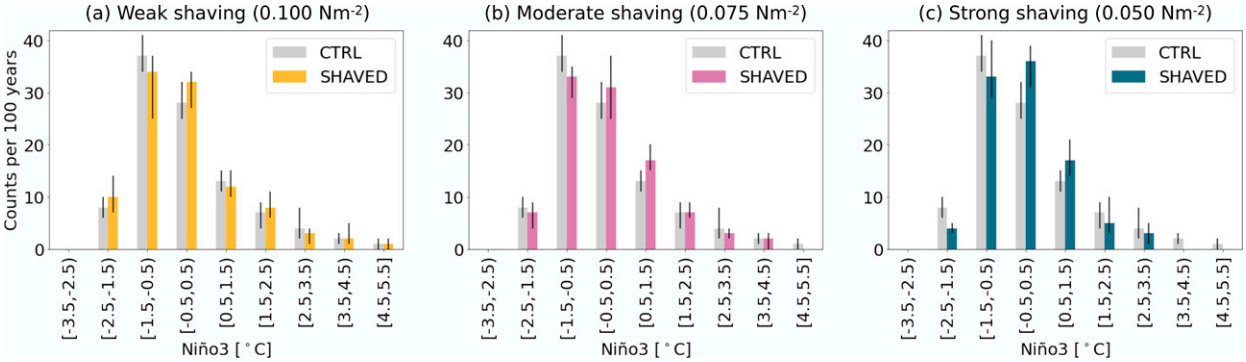

FIG. 10. Histograms of Niño-3 SST, NDJ-averaged, for the (a) weak, (b) moderate, and (c) strong shaving simulations and compared to the Control (gray bars). The bars and whiskers show medians and 90% confidence intervals for each bin, obtained by a block bootstrap method with 100 000 resamplings of 100-yr segments with an 80-yr overlap. Note the reduction of extreme EP El Niño events (amplitude ≥ 2.5°C) in all wind shaving experiments. For the strong wind shaving, the reduction happens for all strong events (amplitude ≥ 1.5°C). The number of La Niña events decreases as well.

decreases monotonically with wind stress shaving, while the mean values of Niño-3 SST (colored dashed lines) do not change relative to the control simulation (gray dashed line). As a result, ENSO skewness decreases for stronger wind shaving, making the distribution more symmetric. The excess kurtosis of the distribution (i.e., kurtosis minus three) also decreases and becomes negative due to the reduction of extreme El Niño and the concurrent increase of the frequency of weak El Niño events.

c. *Individual El Niño events*

In this section, we compare individual El Niño events across the wind shaving simulations. The three categories of ENSO years are compared: neutral (|NDJ Niño-3| ≤ 0.5°C), moderately strong El Niño (NDJ Niño-3 ≈ 3°C, which corresponds to 2.2 times the standard deviation of the control simulation), and top-1% El Niño (NDJ Niño-3 ≥ the 99th percentile). One event satisfying the above conditions is randomly chosen from each simulation and displayed in Fig. 12. In this figure, columns and rows are arranged by simulations and ENSO categories, respectively. Each subpanel shows Hovmöller diagrams for daily zonal wind stress anomalies from the atmospheric model ($\tau'_{x,\mathrm{atm}}$; left) and from the ocean model ($\tau'_{x,\mathrm{ocn}}$; center), and for daily sea surface temperature anomalies (SST′; right). We remind the reader that the wind shaving procedure is applied only to the wind stress that the ocean feels, and accordingly $\tau'_{x,\mathrm{ocn}}$ describes shaved wind stress anomalies versus the original $\tau'_{x,\mathrm{atm}}$.

The wind shaving procedure has little impacts during ENSO-neutral years. Figures 12a–c show ENSO-neutral years from the perturbed experiments. In fact, in all wind shaving simulations, the $\tau'_{x,\mathrm{atm}}$ and $\tau'_{x,\mathrm{ocn}}$ fields look indistinguishable during ENSO-neutral years, since WWBs are not frequently observed during ENSO-neutral years. The SST′ fields also look indistinguishable across different simulations in these panels.

Moderately strong El Niño events can still develop even under strong wind shaving, although the likelihood of their occurrence might be reduced (e.g., Yu and Fedorov 2020). Figures 12d–f show the years of moderately strong El Niño

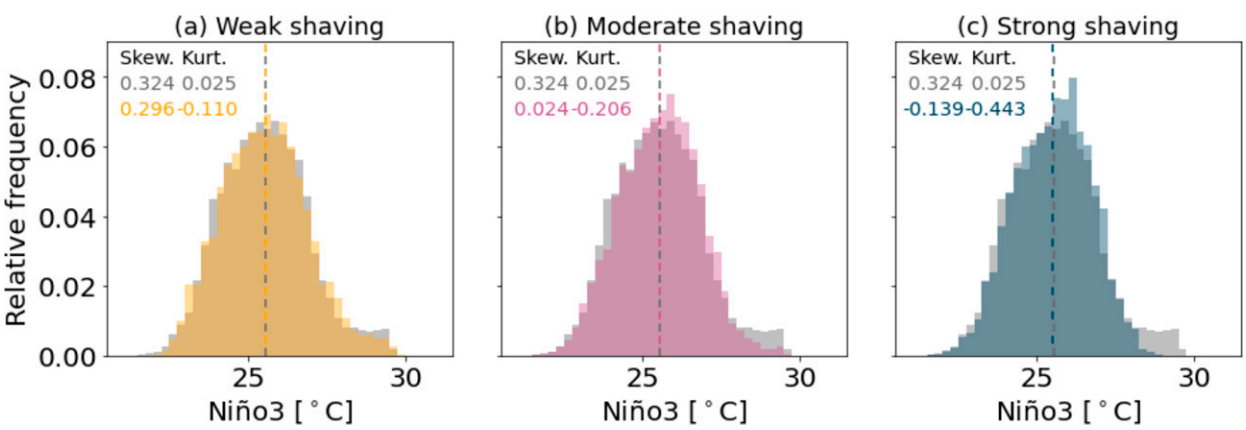

FIG. 11. Histograms of monthly Niño-3 SST variations in the (a) weak, (b) moderate, and (c) strong shaving simulations. A 3-month running mean is applied and the annual cycle is not subtracted from the data before the computations. Dashed lines show mean values, and skewness and excess kurtosis (kurtosis minus three) are provided at the top-left corner of each panel. The histogram for the control simulation is shown in gray.

Unauthenticated | Downloaded 02/21/24 12:34 PM UTC

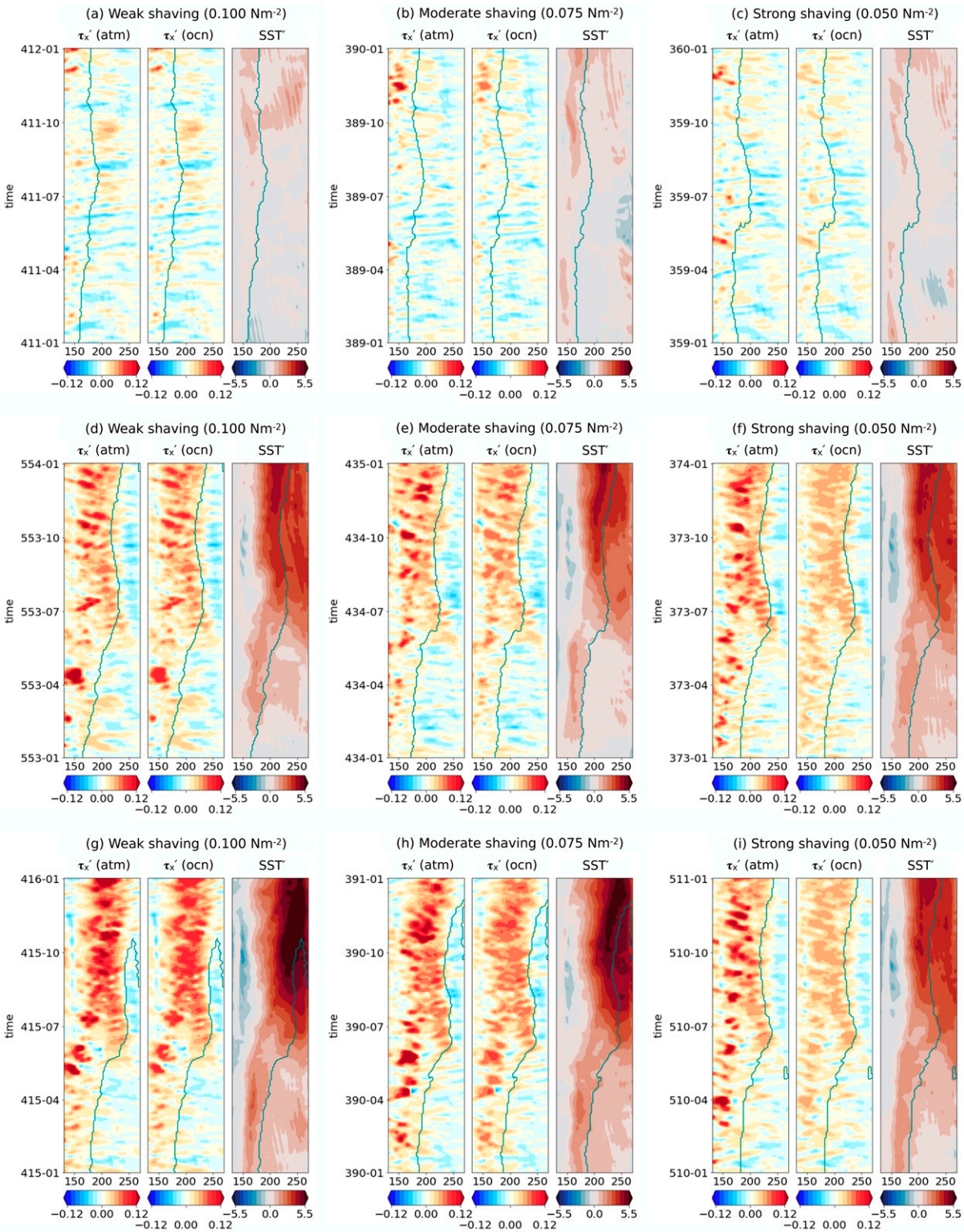

FIG. 12. Each set of three Hovmöller diagrams shows (left) daily zonal surface wind stress anomalies τ_x' from the atmospheric model, (center) "shaved" τ_x' from the ocean model, and (right) daily sea surface temperature anomalies, SST′ in the equatorial Pacific Ocean (2°S–2°N). (a)–(c) Randomly chosen ENSO-neutral years (NDJ Niño-3 index below 0.5°C) in the weak, moderate, and strong shaving simulations, respectively. (d)–(f) As in (a)–(c), but for strong El Niño years (NDJ Niño-3 index of about 3°C). (g)–(i) As in (d)–(f), but for top-1% El Niño years in the model (NDJ Niño-3 index above the 99th percentile for a given simulation). The position of the eastern edge of the warm pool (the 28°C isotherm) is shown as a green contour in (g)–(i).

Unauthenticated | Downloaded 02/21/24 12:34 PM UTC

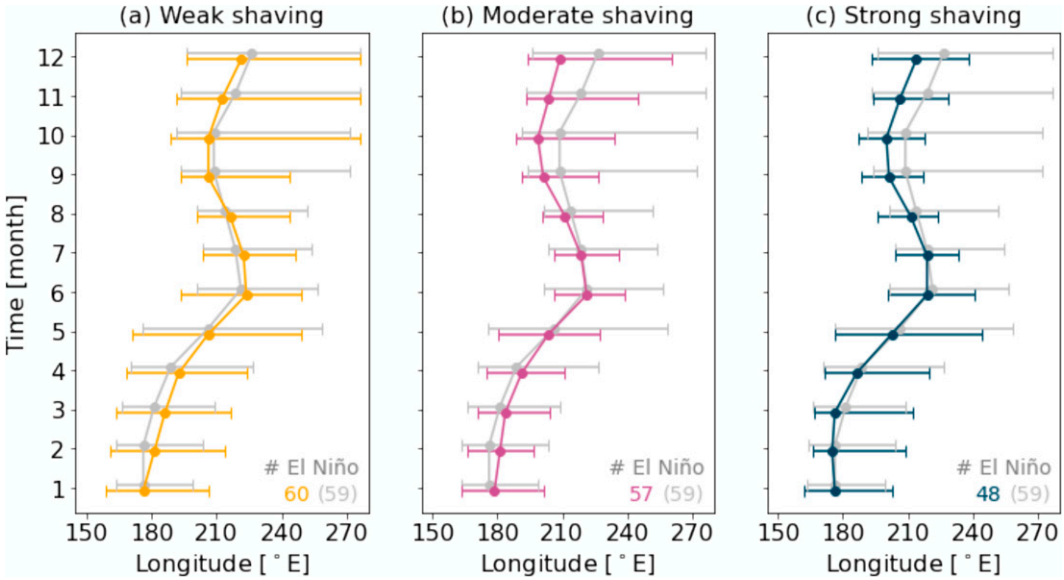

FIG. 13. The monthly location of the eastern edge of the Pacific warm pool at the equator (2°S–2°N) during El Niño events in the (a) weak, (b) moderate, and (c) strong shaving simulations. The control simulation is shown in gray. Dots represent median values; error bars indicate the range between the 5th and the 95th percentiles. The warm pool edge is defined as the 28°C isotherm of SST. The numbers of qualified El Niño events (with amplitudes greater than one standard deviation of NDJ Niño-3 SST anomaly of the control simulation) are shown at the bottom-right corner of each panel. Removing WWBs suppresses the Pacific warm pool eastward expansion in the second half of the year critical for El Niño development.

events from the perturbed simulations. While those events in the weak shaving simulation do not exhibit much difference (Fig. 12d), El Niño events in the moderate and strong shaving simulations (Figs. 12e,f) show noticeable effects of wind shaving on the daily zonal wind stress fields as seen from the difference between $\tau'_{x,\mathrm{atm}}$ and $\tau'_{x,\mathrm{ocn}}$. Regardless of the strength of wind shaving, moderately strong El Niño can still develop. More generally, the intraseasonal component of wind forcing such as WWBs appears to be not critical for the existence of El Niño events up to this magnitude (about 2 times the standard deviation) in this model.

In contrast to moderately strong El Niño events, the role of WWBs turns out to be critical for extreme El Niño events, as indicated by the histograms of Niño-3 indices (Fig. 10). In addition, Figs. 12g–i show top-1% El Niño events in the perturbed simulations. The magnitude of the strongest El Niño events varies; the 99th percentile NDJ-mean Niño-3 index decreases monotonically with the strength of wind stress shaving (Fig. 10). Another noticeable difference is the different location of WWBs in the middle of the year for different experiments, whereas all WWBs in the early part of year reside in the western/central Pacific. Finally, although WWBs generated by the atmospheric model are active throughout the year regardless of the degree of wind shaving, a stronger shaving limits the eastward migration of WWBs as El Niño develops.

d. *The WWB–warm pool feedback*

The aforementioned results highlight the positive intraseasonal feedback that links WWBs and the Pacific warm pool eastward migration (e.g., Lengaigne et al. 2004; Fedorov et al. 2015; Hu and Fedorov 2019; Puy et al. 2019) and its role in the development of extreme El Niño. The eastern boundary of the western Pacific warm pool (defined as the 28°C isotherm; hereafter referred to as the warm pool eastern edge) is overlaid as a dark green contour in Figs. 12g–i. In the strong shaving simulation, the warm pool eastern edge stays in the western and central Pacific throughout the development of El Niño. In contrast, the warm pool eastern edge can reach the eastern Pacific in the weak and moderate shaving simulations, although the arrival of the warm pool edge to the South American coast may happen later in the year in the moderate shaving simulation.

Figure 13 shows the monthly mean median (dots) and 90% confidence intervals (a range between the 5th and the 95th percentiles; error bars) for the warm pool eastern edge's location for El Niño events whose NDJ Niño-3 indices are larger than one standard deviation of the control simulation (1.37°C). Comparing the shift of the median of the warm pool edge with the control indicates that the wind stress shaving procedure clearly restricts the eastward migration of the warm pool during El Niño development in the second half of the year.

In contrast, the eastward migration of the warm pool edge during the first half of the year appears to be insensitive to the removal of WWB wind stress (although this does not necessarily imply that early-year WWBs are not important). These results confirm the importance of midyear WWBs in the development of strong El Niño events (Puy et al. 2019; Hu and Fedorov 2019; Yu and Fedorov 2020). Interestingly, the monthly migration of the medians is similar between the

Unauthenticated | Downloaded 02/21/24 12:34 PM UTC

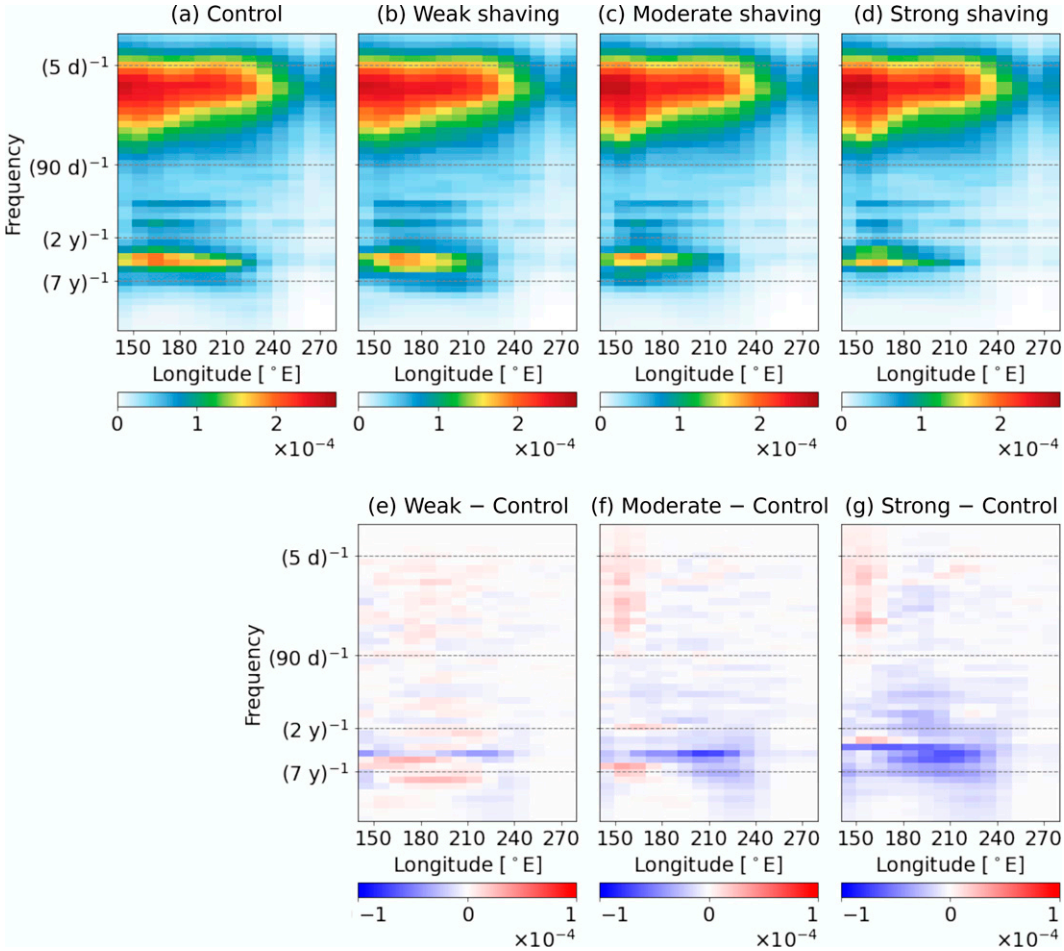

FIG. 14. Power spectra of daily zonal surface wind stress anomalies [(N m^{-2})^2] generated by the atmospheric model in the equatorial Pacific for (a) the control and the (b) weak, (c) moderate, and (d) strong shaving experiments. (e)–(g) The difference between the wind shaving simulations and the control. The power spectra are averaged in consecutive 10° longitude segments and shown in a "variance-preserving" form, i.e., the power spectral density is multiplied by frequency and the frequency axes use a natural logarithmic scale. To estimate power spectral density a multitaper method is used (Thomson 1982; Park et al. 1987). Wind stress is averaged between 5°S and 5°N.

moderate and strong shaving simulations, but the spread (error bars) and the 95th percentile (the maximum extent of error bars) are widely different, again pointing to the importance of WWBs in the migration of the warm pool edge and the corresponding positive ocean–atmosphere feedback during strong El Niño events. Therefore, this positive feedback should be treated as part of the Bjerknes feedback that controls El Niño growth.

5. Discussion

The primary objective of the wind shaving approach is to limit the effect of WWB wind stress variations that the ocean feels while maintaining intraseasonal variability of atmospheric surface winds. To confirm that intraseasonal surface wind variations on WWB time scales are not affected by the wind shaving procedure, we compute longitudinally resolved power spectra of daily surface zonal wind stress anomalies produced by the atmospheric model (Fig. 14). This figure shows the power spectral density of daily equatorial (5°S–5°N mean) zonal surface wind stress anomalies averaged for consecutive 10° longitude segments for the control and the perturbation simulations. Most of the daily wind variability is concentrated in two bands, intraseasonal (5–90 days) or ENSO (2–7 years); the two weaker peaks at roughly 10 and 15 months are combination modes that arise from the interaction between ENSO and the annual cycle (Stuecker et al. 2013). Figures 14e–g display the difference between the control and the wind shaving simulations.

Spectral power in the intraseasonal band shows only minimal changes under wind shaving. The weak shaving experiment shows no notable changes (Fig. 14e), while the moderate and strong shaving simulations show a slight shift of power density from the central to the western Pacific (Figs. 14f,g), which might be related to restricted eastward migration of WWBs during the development of El Niño

Unauthenticated | Downloaded 02/21/24 12:34 PM UTC

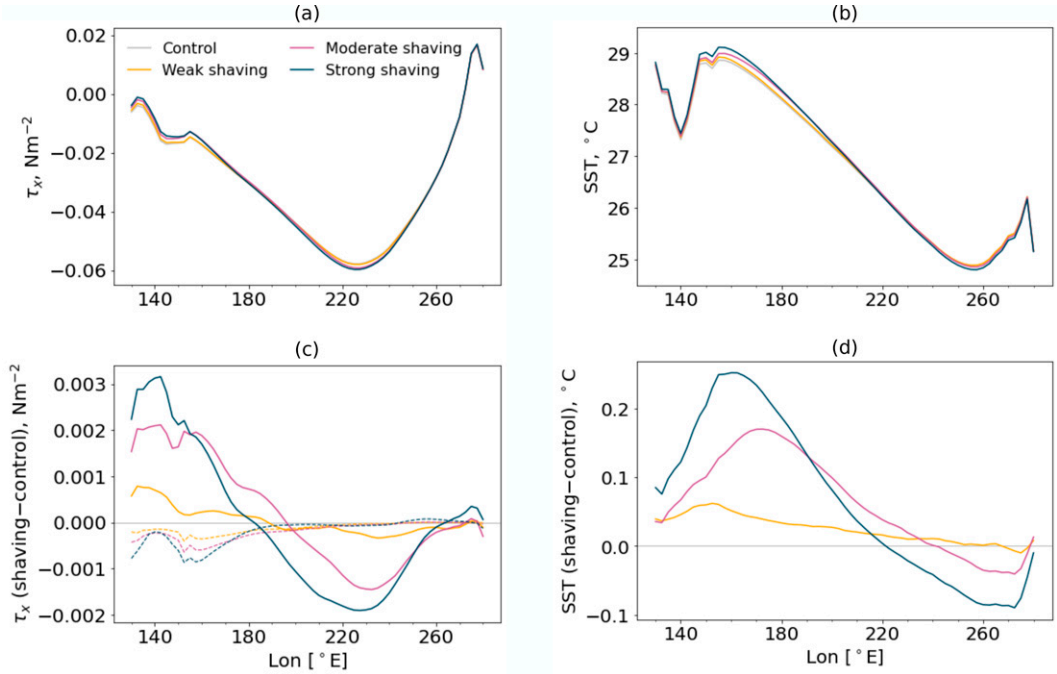

FIG. 15. Profiles of climatological annual-mean (a) zonal surface wind stress (τ_x) and (b) SST along the equator in the wind shaving and control experiments, and (c),(d) the corresponding mean state anomalies in the wind shaving experiments relative to the control. SST and wind stress are averaged between 5°S–5°N and over 400 years. The estimated differences between the mean states of the experiments are small. Differences between climatological annual cycles in the experiments are plotted in Figs. S8 and S9. In addition, dashed lines in (c) show long-term mean residual τ_x anomalies in the equatorial Pacific that would arise when the shaving procedure is applied offline to the wind stress of the control simulation (i.e., without any further adjustment of the system). These mean residuals have a different structure and much smaller amplitudes than the already small rectification of the mean state (solid lines) that occurs in the wind shaving experiments due to ocean–atmosphere coupling.

(Figs. 12g–i). By contrast, spectral power in the interannual band shows systematic weakening in the moderate and strong shaving simulations (Figs. 14f,g), but only minor changes under weak wind shaving (Fig. 14e). The reduction of spectral power density in the interannual band is consistent with the weakened ENSO (Figs. 7 and 8).

Next, we examine potential changes in the mean state (background climate) of the equatorial Pacific Ocean caused by the wind shaving procedure. Such changes could result from mean state rectification caused by ENSO nonlinearity (Rodgers et al. 2004; Ogata et al. 2013; Choi et al. 2013; Kohyama et al. 2017) or might be due to nonlinear aspects of the wind shaving procedure. In turn, ENSO properties can be further affected by these changes in the mean state (Fedorov and Philander 2000; Wang and An 2002; Zhao and Fedorov 2020; Fedorov et al. 2021). Acknowledging the possibility of this two-way interaction between the mean state and ENSO, we therefore need to evaluate mean state changes over the equatorial Pacific.

The climatological annual-mean zonal surface wind stress (τ_x) and SST over the equatorial Pacific Ocean are shown in Fig. 15 (note that τ_x plotted in this figure is given by the atmosphere model and hence not shaved). The background state changes induced in the perturbation experiments are systematic but small as compared to the standard deviation of annual mean (Fig. S7). In addition, these background state changes do not have preferable seasons with a particularly large response (Figs. S8 and S9). The pattern of the mean state changes is La Niña–like; that is, SST warms in the western Pacific and cools in the eastern Pacific (Figs. 15b,d). Consistent with mean SST changes, background τ_x develops mean westerly and easterly wind anomalies in the western and eastern equatorial Pacific, respectively (Figs. 15a,c). This mean La Niña–like response under the wind shaving is likely due to a weaker ENSO and, specifically, less frequent extreme El Niño events. We note that the annual-mean Niño-3 SST is indistinguishable between the wind shaving and the control simulations, but the frequencies of extreme El Niño are noticeably different (Fig. 11).

Likewise, the subsurface structures of the equatorial Pacific show subtle La Niña–like mean changes under the wind shaving (Fig. 16). Nevertheless, despite the small temperature anomalies in the upper ocean, the depth and slope of the equatorial Pacific thermocline (e.g., the 20°C isotherm) in all three perturbation experiments are indistinguishable from those in the control simulation. Overall, these long-term changes in the mean state appear to be an order of magnitude too small to cause noticeable changes in ENSO. Previous work using CESM1.2 (Zhao and Fedorov 2020) has shown that much greater changes in the zonal winds and/or the equatorial ocean thermal structure would be

Unauthenticated | Downloaded 02/21/24 12:34 PM UTC

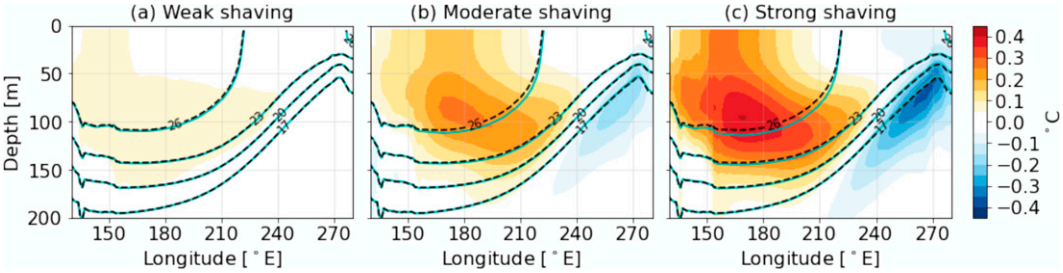

FIG. 16. Mean changes (color shading) in annual-mean upper-ocean temperature along the equator in the (a) weak, (b) moderate, and (c) strong shaving simulations, relative to the control. Shading intervals are 0.05°C. The contours show isotherms for the perturbed (cyan) and control (black dashed lines) experiments. Temperature is averaged between 5°S and 5°N. The averaging time period is 400 years.

needed to induce ENSO changes comparable to the observed in our wind shaving experiments. In their study, a reduction of Niño-3 variability (standard deviation) by 0.4°C resulted from imposing anomalous easterlies (-0.018 N m^{-2} at the largest). In comparison, in our strong shaving simulation the Niño-3 variability is reduced by the same order of magnitude (by 0.26°C; Fig. 6b), while the change to the mean zonal wind stress is an order of magnitude smaller than in Zhao and Fedorov (from -0.002 to 0.003 N m^{-2}; Fig. 14c), implying that the changes of the mean-state surface wind in the strong shaving experiment are an order of magnitude too weak to cause the observed weakening of ENSO. In addition, Zhao and Fedorov (2020) documented a deepening of the thermocline in the western and central Pacific by about 30 m as a result of the mean state wind change, but the wind shaving procedure does not induce any noticeable change of the thermocline structure as stated above.

There is yet another possibility, namely that the estimated mean state changes might have been caused directly by net nonzero wind stress anomalies associated with the wind shaving procedure as it removes more WWBs than EWBs (Fig. 4; see also Fig. S2). To investigate this possibility, we estimate residual mean wind stress anomalies generated by applying wind shaving to the control simulation (Fig. 15c; see also Fig. S10). We find that the long-term mean residuals of intraseasonal wind stress anomalies are a factor of 3 or 4 smaller—and have a very different spatial structure—than the actual mean wind stress changes (Fig. 15c). This result suggests that the rectification effect due to ENSO nonlinearities is the primary cause of the observed mean state changes.

Thus, these findings confirm that the changes of ENSO characteristics in our wind shaving simulations are indeed caused by the reduction of WWB wind stress acting on the ocean rather than by changes in atmospheric intraseasonal wind variability or changes in the mean state of the tropical Pacific.

6. Summary and conclusions

In this study, the role of WWBs in ENSO characteristics and extreme El Niño event frequency has been investigated using "wind shaving" climate model experiments. In the wind shaving simulations, zonal momentum transfer from the atmosphere to the ocean (i.e., zonal surface wind stress associated with WWBs) is reduced to match a prescribed threshold. That is, the effect of strong surface wind variations to the ocean is "shaved." We have completed three wind shaving perturbation experiments with different strengths of wind shaving as indicated by the experiment's name (weak, moderate, and strong shaving simulations). The long model integrations (each lasting 400 years), minimizing the influence of multidecadal ENSO modulation, reveal major systematic effects of WWBs on ENSO as summaries below. Our findings echo the results of previous studies, but we emphasize that unlike those studies, the wind shaving experiments 1) limit changes to the tropical Pacific mean state in a fully coupled GCM and 2) reduce the effects of intrinsic, model-generated WWBs and hence enable us to rigorously quantify the WWB effects on ENSO.

Limiting WWB wind stress weakens ENSO monotonically in accordance with the strength of wind shaving, agreeing with several previous studies (e.g., Fedorov 2002; Eisenman et al. 2005; Gebbie et al. 2007; Lopez and Kirtman 2013; Hu and Fedorov 2019; Puy et al. 2019). The standard deviation of daily Niño-3 SST anomalies is reduced to 98%, 87%, and 78% for the weak, moderate, and strong shaving simulations. In the strong wind stress shaving experiment, we remove most of the WWB wind stress effect on the ocean, while still not affecting more gradual wind stress variations. Consequently, eliminating the cumulative effect of WWBs leads to the reduction of ENSO Niño-3 SST amplitude by about 22%. The maximum SST standard deviation along the equator decreases even more, by over a quarter. Along with the weakening of ENSO, the spatial pattern of El Niño events is also affected—on average the warming center of El Niño shifts westward under wind shaving, and the magnitude and the frequency of EP El Niño decreases. The westward shift of El Niño warming pattern under reduced WWBs is in agreement with previous findings (e.g., Lopez and Kirtman 2013; Hu et al. 2014; Lian et al. 2014; Chen et al. 2015; Fedorov et al. 2015; Thual et al. 2016; Hayashi and Watanabe 2017).

Limiting WWB dynamical effects has a particularly strong impact on the frequency of extreme El Niño events, confirming the role of WWBs in the development of extreme El Niño events (e.g., Lopez et al. 2013; Fedorov et al. 2015; Levine et al. 2016; Hu and Fedorov 2019; Puy et al. 2019; Yu and

Unauthenticated | Downloaded 02/21/24 12:34 PM UTC

Fedorov 2020). While the weak shaving simulation does not produce noticeable changes, the moderate and strong shaving experiments exhibit systematic decrease in the frequency of extreme El Niño events; for example, these experiments no longer simulate El Niño events with amplitude stronger than 4.5° and 3.5°C, respectively, within 400-yr model integrations. Such events are present in the control simulation. The reduced frequency of extreme El Niño events and the concurrent increase in the frequency of weaker El Niño events make ENSO less asymmetric.

In addition, the frequency of strong La Niña events in the perturbation experiments decreases as well. One potential factor contributing to the reduction of strong La Niña events is that the wind shaving procedure is also applied to EWBs (to reduce potential changes to the mean state of the equatorial Pacific). Another potential factor is the reduced occurrence of extreme El Niño events. Such events typically cause a large ocean heat discharge that often leads to strong La Niña events. Investigating EWBs and La Niña is an important topic, but it lies beyond the scope of this study.

The positive ocean–atmosphere feedback between WWBs and the tropical Pacific warm pool operating on intraseasonal time scales is shown to be crucial for the development of extreme El Niño events and hence should be considered as part of the Bjerknes feedback, corroborating previous studies that examined interactions between SST and WWBs (e.g., McPhaden 1999; Vecchi and Harrison 2000; Yu et al. 2003; Lengaigne et al. 2004; Eisenman et al. 2005; Tziperman and Yu 2007; Seiki and Takayabu 2007a; Levine et al. 2017; Hu and Fedorov 2019). The weak shaving experiment shows that the Pacific warm pool eastward migration during El Niño events is practically indistinguishable from that in the control simulation; however, the moderate shaving and especially the strong shaving experiments show much more limited eastward warm pool migrations, never reaching the far eastern equatorial Pacific. On the other hand, moderately strong El Niño events (up to 2.2 times the standard deviation of NDJ Niño-3 anomalies) can develop even in the strong shaving experiment, suggesting that model WWBs are not necessarily critical for the development of moderately strong and weaker El Niño events.

We have also demonstrated that the induced changes in ENSO in the wind shaving experiments arise as a direct consequence of limiting the effect of WWB wind stress anomalies on the ocean, and not because of changes in atmospheric intraseasonal wind variability itself or changes in the background climate state of the equatorial Pacific. The power spectra of atmospheric surface wind show minimal differences in the intraseasonal band, which indicates that WWBs generated by the atmosphere are not affected by the wind stress shaving procedure. Likewise, the mean state of the equatorial Pacific shows only very small, La Niña–like changes in background SST and zonal surface winds under the wind shaving. Given very small changes in the equatorial SST and the ocean thermocline, this background state response is likely caused by the reduced frequency of extreme El Niño events via a mean state rectification.

In this study, we have demonstrated the importance of WWBs in modulating the frequency and intensity of extreme El Niño and other ENSO characteristics (e.g., nonlinearity and asymmetry, spatial diversity, and ENSO rectification of the mean state) in a global climate model. Our results further imply that future changes in WWBs could alter the frequency of extreme El Niño events and other ENSO characteristics. How will WWBs change under global warming (WWB duration, location, fetch, and intensity)? Could those future changes increase the frequency of extreme El Niño? These are the topics of an ongoing complementary study.

Acknowledgments. We acknowledge funding support from NASA (NNX17AH21G), NOAA (NA20OAR4310377), DOE (DE-SC0023134), and a generous gift to Yale University from Todd Sandoz. Additional funding is provided by the ARCHANGE project (ANR-18-MPGA-0001, France). We would like to acknowledge high-performance computing support from Cheyenne and Casper (https://doi.org/10.5065/D6RX99HX) provided by NCAR's Computational and Information Systems Laboratory, sponsored by the National Science Foundation, and from Grace provided by Yale Center for Research Computing. We also thank Billy Kessler (NOAA PMEL) for useful discussions and two anonymous reviewers and the editor for their constructive comments that improved the logic and clarity of the initial manuscript.

Data availability statement. The CESM simulation output used in this study is available in the Dryad repository at https://doi.org/10.5061/dryad.vhhmgqnxm. The ERA-Interim dataset can be assessed from https://www.ecmwf.int/en/forecasts/datasets/reanalysis-datasets/era-interim/ and the MERRA-2 data are available at https://gmao.gsfc.nasa.gov/reanalysis/MERRA-2/data_access/.

REFERENCES

An, S., E. Tziperman, Y. M. Okumura, and T. Li, 2021: ENSO irregularity and asymmetry. *El Niño Southern Oscillation in a Changing Climate, Geophys. Monogr.*, Vol. 253, Wiley, 153–172.

Bellenger, H., E. Guilyardi, J. Leloup, M. Lengaigne, and J. Vialard, 2014: ENSO representation in climate models: From CMIP3 to CMIP5. *Climate Dyn.*, **42**, 1999–2018, https://doi.org/10.1007/s00382-013-1783-z.

Bjerknes, J., 1969: Atmospheric teleconnections from the equatorial Pacific. *Mon. Wea. Rev.*, **97**, 163–172, https://doi.org/10.1175/1520-0493(1969)097<0163:ATFTEP>2.3.CO;2.

Burls, N., L. Muir, E. M. Vincent, and A. Fedorov, 2017: Extratropical origin of equatorial Pacific cold bias in climate models with links to cloud albedo. *Climate Dyn.*, **49**, 2093–2113, https://doi.org/10.1007/s00382-016-3435-6.

Capotondi, A., and Coauthors, 2015: Understanding ENSO diversity. *Bull. Amer. Meteor. Soc.*, **96**, 921–938, https://doi.org/10.1175/BAMS-D-13-00117.1.

——, C. Deser, A. S. Phillips, Y. Okumura, and S. M. Larson, 2020: ENSO and Pacific decadal variability in the Community Earth System Model version 2. *J. Adv. Model. Earth Syst.*, **12**, e2019MS002022, https://doi.org/10.1029/2019MS002022.

Unauthenticated | Downloaded 02/21/24 12:34 PM UTC

Chen, D., and Coauthors, 2015: Strong influence of westerly wind bursts on El Niño diversity. *Nat. Geosci.*, **8**, 339–345, https://doi.org/10.1038/ngeo2399.

Chiodi, A. M., and D. E. Harrison, 2015: Equatorial Pacific easterly wind surges and the onset of La Niña events. *J. Climate*, **28**, 776–792, https://doi.org/10.1175/JCLI-D-14-00227.1.

——, ——, and G. A. Vecchi, 2014: Subseasonal atmospheric variability and El Niño waveguide warming: Observed effects of the Madden–Julian oscillation and westerly wind events. *J. Climate*, **27**, 3619–3642, https://doi.org/10.1175/JCLI-D-13-00547.1.

Choi, J., S.-I. An, S.-W. Yeh, and J.-Y. Yu, 2013: ENSO-like and ENSO-induced tropical Pacific decadal variability in CGCMs. *J. Climate*, **26**, 1485–1501, https://doi.org/10.1175/JCLI-D-12-00118.1.

Chu, P.-S., 1988: Extratropical forcing and the burst of equatorial westerlies in the western Pacific: A synoptic study. *J. Meteor. Soc. Japan*, **66**, 549–564, https://doi.org/10.2151/jmsj1965.66.4_549.

Dee, D. P., and Coauthors, 2011: The ERA-Interim reanalysis: Configuration and performance of the data assimilation system. *Quart. J. Roy. Meteor. Soc.*, **137**, 553–597, https://doi.org/10.1002/qj.828.

Delcroix, T., G. Eldin, M. McPhaden, and A. Morlière, 1993: Effects of westerly wind bursts upon the western equatorial Pacific Ocean, February–April 1991. *J. Geophys. Res.*, **98**, 16 379–16 385, https://doi.org/10.1029/93JC01261.

DiNezio, P. N., C. Deser, Y. Okumura, and A. Karspeck, 2017: Predictability of 2-year La Niña events in a coupled general circulation model. *Climate Dyn.*, **49**, 4237–4261, https://doi.org/10.1007/s00382-017-3575-3.

Eisenman, I., L. Yu, and E. Tziperman, 2005: Westerly wind bursts: ENSO's tail rather than the dog? *J. Climate*, **18**, 5224–5238, https://doi.org/10.1175/JCLI3588.1.

Fedorov, A. V., 2002: The response of the coupled tropical ocean–atmosphere to westerly wind bursts. *Quart. J. Roy. Meteor. Soc.*, **128**, 1–23, https://doi.org/10.1002/qj.200212857901.

——, and S. G. Philander, 2000: Is El Niño changing? *Science*, **288**, 1997–2002, https://doi.org/10.1126/science.288.5473.1997.

——, S. L. Harper, S. G. Philander, B. Winter, and A. Wittenberg, 2003: How predictable is El Niño? *Bull. Amer. Meteor. Soc.*, **84**, 911–920, https://doi.org/10.1175/BAMS-84-7-911.

——, S. Hu, M. Lengaigne, and E. Guilyardi, 2015: The impact of westerly wind bursts and ocean initial state on the development, and diversity of El Niño events. *Climate Dyn.*, **44**, 1381–1401, https://doi.org/10.1007/s00382-014-2126-4.

——, ——, A. T. Wittenberg, A. F. Z. Levine, and C. Deser, 2021: ENSO low-frequency modulation and mean state interactions. *El Niño Southern Oscillation in a Changing Climate. Geophy. Monogr.*, Vol. 253, Wiley, 173–198.

Feng, J., and T. Lian, 2018: Assessing the relationship between MJO and equatorial Pacific WWBs in observations and CMIP5 models. *J. Climate*, **31**, 6393–6410, https://doi.org/10.1175/JCLI-D-17-0526.1.

Gebbie, G., and E. Tziperman, 2009: Incorporating a semi-stochastic model of ocean-modulated westerly wind bursts into an ENSO prediction model. *Theor. Appl. Climatol.*, **97**, 65–73, https://doi.org/10.1007/s00704-008-0069-6.

——, I. Eisenman, A. Wittenberg, and E. Tziperman, 2007: Modulation of westerly wind bursts by sea surface temperature: A semistochastic feedback for ENSO. *J. Atmos. Sci.*, **64**, 3281–3295, https://doi.org/10.1175/JAS4029.1.

Gelaro, R., and Coauthors, 2017: The Modern-Era Retrospective Analysis for Research and Applications, version 2 (MERRA-2). *J. Climate*, **30**, 5419–5454, https://doi.org/10.1175/JCLI-D-16-0758.1.

Guilyardi, E., W. Cai, M. Collins, A. Fedorov, F.-F. Jin, A. Kumar, D.-Z. Sun, and A. Wittenberg, 2012: New strategies for evaluating ENSO processes in climate models. *Bull. Amer. Meteor. Soc.*, **93**, 235–238, https://doi.org/10.1175/BAMS-D-11-00106.1.

Harrison, D. E., 1984: The appearance of sustained equatorial surface westerlies during the 1982 Pacific warm event. *Science*, **224**, 1099–1102, https://doi.org/10.1126/science.224.4653.1099.

——, and D. S. Luther, 1990: Surface winds from tropical Pacific islands—Climatological statistics. *J. Climate*, **3**, 251–271, https://doi.org/10.1175/1520-0442(1990)003<0251:SWFTPI>2.0.CO;2.

——, and B. S. Giese, 1991: Episodes of surface westerly winds as observed from islands in the western tropical Pacific. *J. Geophys. Res.*, **96**, 3221–3237, https://doi.org/10.1029/90JC01775.

Hartten, L. M., 1996: Synoptic settings of westerly wind bursts. *J. Geophys. Res.*, **101**, 16 997–17 019, https://doi.org/10.1029/96JD00030.

Hayashi, M., and M. Watanabe, 2016: Asymmetry of westerly and easterly wind events: Observational evidence. *SOLA*, **12**, 42–45, https://doi.org/10.2151/sola.2016-009.

——, and ——, 2017: ENSO complexity induced by state dependence of westerly wind events. *J. Climate*, **30**, 3401–3420, https://doi.org/10.1175/JCLI-D-16-0406.1.

Hu, S., and A. V. Fedorov, 2016: Exceptionally strong easterly wind burst stalling El Niño of 2014. *Proc. Natl. Acad. Sci. USA*, **113**, 2005–2010, https://doi.org/10.1073/pnas.1514182113.

——, and ——, 2019: The extreme El Niño of 2015–2016: The role of westerly and easterly wind bursts, and preconditioning by the failed 2014 event. *Climate Dyn.*, **52**, 7339–7357, https://doi.org/10.1007/s00382-017-3531-2.

——, ——, M. Lengaigne, and E. Guilyardi, 2014: The impact of westerly wind bursts on the diversity and predictability of El Niño events: An ocean energetics perspective. *Geophys. Res. Lett.*, **41**, 4654–4663, https://doi.org/10.1002/2014GL059573.

Hurrell, J. W., and Coauthors, 2013: The Community Earth System Model: A framework for collaborative research. *Bull. Amer. Meteor. Soc.*, **94**, 1339–1360, https://doi.org/10.1175/BAMS-D-12-00121.1.

Jin, F.-F., L. Lin, A. Timmermann, and J. Zhao, 2007: Ensemble-mean dynamics of the ENSO recharge oscillator under state-dependent stochastic forcing. *Geophys. Res. Lett.*, **34**, L03807, https://doi.org/10.1029/2006GL027372.

Keen, R. A., 1982: The role of cross-equatorial tropical cyclone pairs in the Southern Oscillation. *Mon. Wea. Rev.*, **110**, 1405–1416, https://doi.org/10.1175/1520-0493(1982)110<1405:TROCET>2.0.CO;2.

Kohyama, T., D. L. Hartmann, and D. S. Battisti, 2017: La Niña–like mean-state response to global warming and potential oceanic roles. *J. Climate*, **30**, 4207–4225, https://doi.org/10.1175/JCLI-D-16-0441.1.

Kug, J.-S., F.-F. Jin, and S.-I. An, 2009: Two types of El Niño events: Cold tongue El Niño and warm pool El Niño. *J. Climate*, **22**, 1499–1515, https://doi.org/10.1175/2008JCLI2624.1.

Larson, S. M., and B. P. Kirtman, 2015: An alternate approach to ensemble ENSO forecast spread: Application to the 2014 forecast. *Geophys. Res. Lett.*, **42**, 9411–9415, https://doi.org/10.1002/2015GL066173.

Latif, M., J. Biercamp, and H. von Storch, 1988: The response of a coupled ocean–atmosphere general circulation model to

Unauthenticated | Downloaded 02/21/24 12:34 PM UTC

wind bursts. *J. Atmos. Sci.*, **45**, 964–979, https://doi.org/10.1175/1520-0469(1988)045<0964:TROACO>2.0.CO;2.

Lau, K.-M., P. Li, C. H. Sui, and T. Nakazawa, 1989: Dynamics of super cloud clusters, westerly wind bursts, 30–60 day oscillations and ENSO: An unified view. *J. Meteor. Soc. Japan*, **67**, 205–219, https://doi.org/10.2151/jmsj1965.67.2_205.

Lengaigne, M., J.-P. Boulanger, C. Menkes, S. Masson, G. Madec, and P. Delecluse, 2002: Ocean response to the March 1997 westerly wind event. *J. Geophys. Res.*, **107**, 8015, https://doi.org/10.1029/2001JC000841.

——, E. Guilyardi, J.-P. Boulanger, C. Menkes, P. Delecluse, P. Inness, J. Cole, and J. Slingo, 2004: Triggering of El Niño by westerly wind events in a coupled general circulation model. *Climate Dyn.*, **23**, 601–620, https://doi.org/10.1007/s00382-004-0457-2.

Levine, A. F. Z., and F.-F. Jin, 2010: Noise-induced instability in the ENSO recharge oscillator. *J. Atmos. Sci.*, **67**, 529–542, https://doi.org/10.1175/2009JAS3213.1.

——, and M. J. McPhaden, 2016: How the July 2014 easterly wind burst gave the 2015–2016 El Niño a head start. *Geophys. Res. Lett.*, **43**, 6503–6510, https://doi.org/10.1002/2016GL069204.

——, F.-F. Jin, and M. J. McPhaden, 2016: Extreme noise-extreme El Niño: How state-dependent noise forcing creates El Niño–La Niña asymmetry. *J. Climate*, **29**, 5483–5499, https://doi.org/10.1175/JCLI-D-16-0091.1.

——, ——, and M. F. Stuecker, 2017: A simple approach to quantifying the noise–ENSO interaction. Part II: The role of coupling between the warm pool and equatorial zonal wind anomalies. *Climate Dyn.*, **48**, 19–37, https://doi.org/10.1007/s00382-016-3268-3.

Li, G., and S.-P. Xie, 2014: Tropical biases in CMIP5 multimodel ensemble: The excessive equatorial Pacific cold tongue and double ITCZ problems. *J. Climate*, **27**, 1765–1780, https://doi.org/10.1175/JCLI-D-13-00337.1.

Lian, T., D. Chen, Y. Tang, and Q. Wu, 2014: Effects of westerly wind bursts on El Niño: A new perspective. *Geophys. Res. Lett.*, **41**, 3522–3527, https://doi.org/10.1002/2014GL059989.

——, and Coauthors, 2018a: Westerly wind bursts simulated in CAM4 and CCSM4. *Climate Dyn.*, **50**, 1353–1371, https://doi.org/10.1007/s00382-017-3689-7.

——, D. Chen, Y. Tang, X. Liu, J. Feng, and L. Zhou, 2018b: Linkage between westerly wind bursts and tropical cyclones. *Geophys. Res. Lett.*, **45**, 11 431–11 438, https://doi.org/10.1029/2018GL079745.

Liang, Y., and A. V. Fedorov, 2021: Linking the Madden–Julian oscillation, tropical cyclones and westerly wind bursts as part of El Niño development. *Climate Dyn.*, **57**, 1039–1060, https://doi.org/10.1007/s00382-021-05757-1.

Lin, J.-L., 2007: The double-ITCZ problem in IPCC AR4 coupled GCMs: Ocean–atmosphere feedback analysis. *J. Climate*, **20**, 4497–4525, https://doi.org/10.1175/JCLI4272.1.

Lopez, H., and B. P. Kirtman, 2013: Westerly wind bursts and the diversity of ENSO in CCSM3 and CCSM4. *Geophys. Res. Lett.*, **40**, 4722–4727, https://doi.org/10.1002/grl.50913.

——, and ——, 2014: WWBs, ENSO predictability, the spring barrier and extreme events. *J. Geophys. Res. Atmos.*, **119**, 10 114–10 138, https://doi.org/10.1002/2014JD021908.

——, ——, E. Tziperman, and G. Gebbie, 2013: Impact of interactive westerly wind bursts on CCSM3. *Dyn. Atmos. Oceans*, **59**, 24–51, https://doi.org/10.1016/j.dynatmoce.2012.11.001.

Love, G., 1985: Cross-equatorial influence of winter hemisphere subtropical cold surges. *Mon. Wea. Rev.*, **113**, 1487–1498, https://doi.org/10.1175/1520-0493(1985)113<1487:CEIOWH>2.0.CO;2.

Luther, D. S., D. E. Harrison, and R. A. Knox, 1983: Zonal winds in the central equatorial Pacific and El Niño. *Science*, **222**, 327–330, https://doi.org/10.1126/science.222.4621.327.

McPhaden, M. J., 1999: Genesis and evolution of the 1997–98 El Niño. *Science*, **283**, 950–954, https://doi.org/10.1126/science.283.5404.950.

——, and X. Yu, 1999: Equatorial waves and the 1997–98 El Niño. *Geophys. Res. Lett.*, **26**, 2961–2964, https://doi.org/10.1029/1999GL004901.

——, H. P. Freitag, S. P. Hayes, B. A. Taft, Z. Chen, and K. Wyrtki, 1988: The response of the equatorial Pacific Ocean to a westerly wind burst in May 1986. *J. Geophys. Res.*, **93**, 10 589–10 603, https://doi.org/10.1029/JC093iC09p10589.

Mechoso, C. R., and Coauthors, 1995: The seasonal cycle over the tropical Pacific in coupled ocean–atmosphere general circulation models. *Mon. Wea. Rev.*, **123**, 2825–2838, https://doi.org/10.1175/1520-0493(1995)123<2825:TSCOTT>2.0.CO;2.

Meinen, C. S., and M. J. McPhaden, 2000: Observations of warm water volume changes in the equatorial Pacific and their relationship to El Niño and La Niña. *J. Climate*, **13**, 3551–3559, https://doi.org/10.1175/1520-0442(2000)013<3551:OOWWVC>2.0.CO;2.

Moore, A. M., and R. Kleeman, 1999: Stochastic forcing of ENSO by the intraseasonal oscillation. *J. Climate*, **12**, 1199–1220, https://doi.org/10.1175/1520-0442(1999)012<1199:SFOEBT>2.0.CO;2.

Nitta, T., 1989: Development of a twin cyclone and westerly bursts during the initial phase of the 1986-87 El Niño. *J. Meteor. Soc. Japan*, **67**, 677–681, https://doi.org/10.2151/jmsj1965.67.4_677.

Ogata, T., S.-P. Xie, A. Wittenberg, and D.-Z. Sun, 2013: Interdecadal amplitude modulation of El Niño–Southern Oscillation and its impact on tropical Pacific decadal variability. *J. Climate*, **26**, 7280–7297, https://doi.org/10.1175/JCLI-D-12-00415.1.

Park, J., C. R. Lindberg, and F. L. Vernon, 1987: Multitaper spectral analysis of high-frequency seismograms. *J. Geophys. Res.*, **92**, 12 675–12 684, https://doi.org/10.1029/JB092iB12p12675.

Penland, C., and P. D. Sardeshmukh, 1995: The optimal growth of tropical sea surface temperature anomalies. *J. Climate*, **8**, 1999–2024, https://doi.org/10.1175/1520-0442(1995)008<1999:TOGOTS>2.0.CO;2.

Perez, C. L., A. M. Moore, J. Zavala-Garay, and R. Kleeman, 2005: A comparison of the influence of additive and multiplicative stochastic forcing on a coupled model of ENSO. *J. Climate*, **18**, 5066–5085, https://doi.org/10.1175/JCLI3596.1.

Perigaud, C. M., and C. Cassou, 2000: Importance of oceanic decadal trends and westerly wind bursts for forecasting El Niño. *Geophys. Res. Lett.*, **27**, 389–392, https://doi.org/10.1029/1999GL010781.

Picaut, J., and T. Delcroix, 1995: Equatorial wave sequence associated with warm pool displacements during the 1986–1989 El Niño–La Niña. *J. Geophys. Res.*, **100**, 18 393–18 408, https://doi.org/10.1029/95JC01358.

Puy, M., J. Vialard, M. Lengaigne, and E. Guilyardi, 2016: Modulation of equatorial Pacific westerly/easterly wind events by the Madden–Julian oscillation and convectively-coupled Rossby waves. *Climate Dyn.*, **46**, 2155–2178, https://doi.org/10.1007/s00382-015-2695-x.

——, and Coauthors, 2019: Influence of westerly wind events stochasticity on El Niño amplitude: The case of 2014 vs. 2015.

Unauthenticated | Downloaded 02/21/24 12:34 PM UTC

Climate Dyn., **52**, 7435–7454, https://doi.org/10.1007/s00382-017-3938-9.

Rodgers, K. B., P. Friederichs, and M. Latif, 2004: Tropical Pacific decadal variability and its relation to decadal modulations of ENSO. *J. Climate*, **17**, 3761–3774, https://doi.org/10.1175/1520-0442(2004)017<3761:TPDVAI>2.0.CO;2.

Seiki, A., and Y. N. Takayabu, 2007a: Westerly wind bursts and their relationship with intraseasonal variations and ENSO. Part I: Statistics. *Mon. Wea. Rev.*, **135**, 3325–3345, https://doi.org/10.1175/MWR3477.1.

——, and ——, 2007b: Westerly wind bursts and their relationship with intraseasonal variations and ENSO. Part II: Energetics over the western and central Pacific. *Mon. Wea. Rev.*, **135**, 3346–3361, https://doi.org/10.1175/MWR3503.1.

——, ——, T. Yasuda, N. Sato, C. Takahashi, K. Yoneyama, and R. Shirooka, 2011: Westerly wind bursts and their relationship with ENSO in CMIP3 models. *J. Geophys. Res.*, **116**, D03303, https://doi.org/10.1029/2010JD015039.

Stuecker, M. F., A. Timmermann, F.-F. Jin, S. McGregor, and H.-L. Ren, 2013: A combination mode of the annual cycle and the El Niño/Southern Oscillation. *Nat. Geosci.*, **6**, 540–544, https://doi.org/10.1038/ngeo1826.

Tan, X., Y. Tang, T. Lian, Z. Yao, X. Li, and D. Chen, 2020a: A study of the effects of westerly wind bursts on ENSO based on CESM. *Climate Dyn.*, **54**, 885–899, https://doi.org/10.1007/s00382-019-05034-2.

——, ——, ——, S. Zhang, T. Liu, and D. Chen, 2020b: Effects of semistochastic westerly wind bursts on ENSO predictability. *Geophys. Res. Lett.*, **47**, e2019GL086828, https://doi.org/10.1029/2019GL086828.

Thomas, M. D., and A. V. Fedorov, 2017: The eastern subtropical Pacific origin of the equatorial cold bias in climate models: A Lagrangian perspective. *J. Climate*, **30**, 5885–5900, https://doi.org/10.1175/JCLI-D-16-0819.1.

Thompson, C. J., and D. S. Battisti, 2001: A linear stochastic dynamical model of ENSO. Part II: Analysis. *J. Climate*, **14**, 445–466, https://doi.org/10.1175/1520-0442(2001)014<0445:ALSDMO>2.0.CO;2.

Thomson, D. J., 1982: Spectrum estimation and harmonic analysis. *Proc. IEEE*, **70**, 1055–1096, https://doi.org/10.1109/PROC.1982.12433.

Thual, S., A. J. Majda, N. Chen, and S. N. Stechmann, 2016: Simple stochastic model for El Niño with westerly wind bursts. *Proc. Natl. Acad. Sci. USA*, **113**, 10 245–10 250, https://doi.org/10.1073/pnas.1612002113.

Tian, B., and X. Dong, 2020: The double-ITCZ bias in CMIP3, CMIP5, and CMIP6 models based on annual mean precipitation. *Geophys. Res. Lett.*, **47**, e2020GL087232, https://doi.org/10.1029/2020GL087232.

Tziperman, E., and L. Yu, 2007: Quantifying the dependence of westerly wind bursts on the large-scale tropical Pacific SST. *J. Climate*, **20**, 2760–2768, https://doi.org/10.1175/JCLI4138a.1.

Vecchi, G. A., and D. E. Harrison, 2000: Tropical Pacific sea surface temperature anomalies, El Niño, and equatorial westerly wind events. *J. Climate*, **13**, 1814–1830, https://doi.org/10.1175/1520-0442(2000)013<1814:TPSSTA>2.0.CO;2.

Wang, B., and S. An, 2002: A mechanism for decadal changes of ENSO behavior: Roles of background wind changes. *Climate Dyn.*, **18**, 475–486, https://doi.org/10.1007/s00382-001-0189-5.

Wyrtki, K., 1975: El Niño—the dynamic response of the equatorial Pacific Ocean to atmospheric forcing. *J. Phys. Oceanogr.*, **5**, 572–584, https://doi.org/10.1175/1520-0485(1975)005<0572:ENTDRO>2.0.CO;2.

Yu, L., and M. M. Rienecker, 1998: Evidence of an extratropical atmospheric influence during the onset of the 1997–98 El Niño. *Geophys. Res. Lett.*, **25**, 3537–3540, https://doi.org/10.1029/98GL02628.

——, R. A. Weller, and T. W. Liu, 2003: Case analysis of a role of ENSO in regulating the generation of westerly wind bursts in the western equatorial Pacific. *J. Geophys. Res.*, **108**, 3128, https://doi.org/10.1029/2002JC001498.

Yu, S., and A. V. Fedorov, 2020: The role of westerly wind bursts during different seasons versus ocean heat recharge in the development of extreme El Niño in climate models. *Geophys. Res. Lett.*, **47**, e2020GL088381, https://doi.org/10.1029/2020GL088381.

Zavala-Garay, J., A. M. Moore, C. L. Perez, and R. Kleeman, 2003: The response of a coupled model of ENSO to observed estimates of stochastic forcing. *J. Climate*, **16**, 2827–2842, https://doi.org/10.1175/1520-0442(2003)016<2827:TROACM>2.0.CO;2.

——, C. Zhang, A. M. Moore, A. T. Wittenberg, M. J. Harrison, A. Rosati, J. Vialard, and R. Kleeman, 2008: Sensitivity of hybrid ENSO models to unresolved atmospheric variability. *J. Climate*, **21**, 3704–3721, https://doi.org/10.1175/2007JCLI1188.1.

Zhang, T., X. Shao, and S. Li, 2017: Impacts of atmospheric processes on ENSO asymmetry: A comparison between CESM1 and CCSM4. *J. Climate*, **30**, 9743–9762, https://doi.org/10.1175/JCLI-D-17-0360.1.

Zhao, B., and A. Fedorov, 2020: The effects of background zonal and meridional winds on ENSO in a coupled GCM The effects of background zonal and meridional winds on ENSO in a coupled GCM. *J. Climate*, **33**, 2075–2091, https://doi.org/10.1175/JCLI-D-18-0822.1.

Unauthenticated | Downloaded 02/21/24 12:34 PM UTC